Monthly Notices of the ROYAL ASTRONOMICAL SOCIETY

MNRAS **524,** 5497–5513 (2023) https://doi.org/10.1093/mnras/stad2060
Advance Access publication 2023 July 12

No redshift evolution in the rest-frame ultraviolet emission line properties of quasars from $z = 1.5$ to $z = 4.0$

Matthew Stepney [1]★ Manda Banerji [1] Paul C. Hewett [2] Matthew J. Temple [3] Amy L. Rankine [4] James H. Matthews [5] and Gordon T. Richards [6]

[1]*School of Physics and Astronomy, University of Southampton, Southampton SO17 1BJ, UK*
[2]*Institute of Astronomy, University of Cambridge, Madingley Road, Cambridge CB3 0HA, UK*
[3]*Instituto de Estudios Astrofísicos, Universidad Diego Portales, Avenida Ejército Libertador 441, Santiago 8370191, Chile*
[4]*Institute for Astronomy, University of Edinburgh, Royal Observatory, Blackford Hill, Edinburgh EH9 3HJ, UK*
[5]*Department of Physics, Astrophysics, University of Oxford, Denys Wilkinson Building, Keble Road, Oxford OX1 3RH, UK*
[6]*Department of Physics, Drexel University, 3141 Chestnut Street, Philadelphia, PA 19104, USA*

Accepted 2023 July 5. Received 2023 June 6; in original form 2023 March 23

ABSTRACT

We analyse the rest-frame ultraviolet (UV) spectra of 2531 high-redshift ($3.5 < z < 4.0$) quasars from the Sloan Digital Sky Survey DR16Q catalogue. In combination with previous work, we study the redshift evolution of the rest-frame UV line properties across the entire redshift range, $1.5 < z < 4.0$. We improve the systemic redshift estimates at $z > 3.5$ using a cross-correlation algorithm that employs high signal-to-noise template spectra spanning the full range in UV emission line properties. We then quantify the evolution of C IV and He II emission line properties with redshift. The increase in C IV blueshifts with cosmological redshift can be fully explained by the higher luminosities of quasars observed at high redshifts. We recover broadly similar trends between the He II equivalent width and C IV blueshift at both $1.5 < z < 2.65$ and $3.5 < z < 4.0$ suggesting that the blueshift depends systematically on the spectral energy density (SED) of the quasar and there is no evolution in the SED over the redshift range $1.5 < z < 4.0$. C IV blueshifts are highest when $L/L_{\rm Edd} \geq 0.2$ and $M_{\rm BH} \geq 10^9$ M$_\odot$ for the entire $1.5 < z < 4.0$ sample. We find that luminosity matching samples as a means to explore the evolution of their rest-frame UV emission line properties is only viable if the samples are also matched in the $M_{\rm BH}$–$L/L_{\rm Edd}$ plane. Quasars at $z \geq 6$ are on average less massive and have higher Eddington-scaled accretion rates than their luminosity-matched counterparts at $1.5 < z < 4.0$, which could explain the observed evolution in their UV line properties.

Key words: line: profiles – quasars: emission lines – quasars: general.

1. INTRODUCTION

The increase in the size of large spectroscopic samples of high-redshift ($z > 1.5$) quasars, with rest-frame ultraviolet (UV) spectra has been rapid over the past decade. The Sloan Digital Sky Survey (SDSS) DR7 catalogue (Schneider et al. 2010) enabled the study of ∼105 000 rest-frame UV to optical quasar spectra, from which Shen et al. (2011) constructed a comprehensive catalogue of line properties. With the subsequent SDSS data releases and the introduction of the Baryon Oscillation Spectroscopic Survey spectrograph, the SDSS DR16Q catalogue now contains over 750 000 quasars (Lyke et al. 2020), marking a near order of magnitude increase from DR7. Looking to ongoing and upcoming quasar surveys, these numbers are continuing to rapidly increase and push to less optically luminous populations, as well as increasing the numbers at high-redshifts—e.g. the Dark Energy Spectroscopic Instrument (DESI; Alexander et al. 2023), which has an expected quasar target density of $\gtrsim$5 × that in SDSS DR7.

Thanks to these large spectroscopic datasets, we are now able to conduct statistical studies of the rest-frame UV spectra, explore the diversity in their emission line properties and study correlations between the continuum and various emission lines (e.g. Sulentic et al. 2007; Richards et al. 2011; Rakshit, Stalin & Kotilainen 2020; Rankine et al. 2020; Brodzeller & Dawson 2022; Rivera et al. 2022; Wu & Shen 2022). Characterizing the emission line properties also enables single-epoch virial black hole mass estimates for large samples, allowing an exploration of how the UV spectral properties connect to fundamental physical properties of the quasars such as bolometric luminosity, black hole mass, and Eddington-scaled accretion rate (e.g. Temple et al. 2023). The widely observed blueshifts seen in the C IVλλ1548, 1550 emission lines of high-redshift, high-luminosity quasars are often interpreted as a signature of outflowing gas in the quasar broad-line region (BLR; Baskin, Laor & Hamann 2015). Statistical studies of UV quasar spectra then enable these outflows to be linked to other quasar properties. For example, the observed anticorrelation between the C IV blueshift and He II λ1640 equivalent width (EW, Baskin, Laor & Stern 2013; Rankine et al. 2020) can be interpreted as a link between the spectral energy density (SED) of the quasar and BLR outflow velocity (Temple et al. 2023).

★ E-mail: ms10g17@soton.ac.uk

In parallel to these developments in characterizing the demographics of quasars at 'cosmic noon' ($1.5 \lesssim z \lesssim 3.5$), the number of quasars at the highest redshifts ($z \gtrsim 5$) has also grown considerably in the last decade (e.g. Bañados et al. 2016; Jiang et al. 2016; Wang et al. 2019; Fan, Banados & Simcoe 2022). A sizeable subset of these also have single-epoch black hole masses measured from rest-frame optical spectra (e.g. De Rosa et al. 2014; Mazzucchelli et al. 2017; Schindler et al. 2020; Farina et al. 2022). These high-redshift quasars are now being targeted as part of ongoing wide-field spectroscopic surveys such as DESI, which has recently confirmed ∼400 new quasars at $4.7 < z < 6.6$ (Yang et al. 2023). These numbers are only expected to increase further with new observations from the 4-metre Multi-Object Spectroscopic Telescope (4MOST; Merloni et al. 2019).

The discovery of the first quasar at $z > 7$ (Mortlock et al. 2011) showed that its rest-frame UV spectrum was very similar to lower redshift quasars, of similar luminosity, but that the C IV blueshift was significantly larger than the other known $z > 2$ quasars. With larger samples becoming available at high-redshifts, there have been suggestions that high-redshift quasars might in general display stronger C IV blueshifts (e.g. Meyer, Bosman & Ellis 2019; Schindler et al. 2020), as well as higher broad absorption line fractions and velocities (e.g. Bischetti et al. 2022, 2023). However, these samples are still small enough that these results might be affected by limited sample statistics (e.g. Reed et al. 2019; Yang et al. 2021). While there is an indication that there could be a real evolution in the rest-frame UV line properties driven by fundamental differences in the super massive black hole (SMBH) population at the highest redshifts, neither the line properties nor the physical properties of quasars have been measured consistently across the entire range in redshift ($1.5 \lesssim z \lesssim 7.0$).

In the radiation line-driven disc wind paradigm, ionized gas opaque to the UV continuum photons emitted by the accretion disc, due to UV line transitions, traces the streamlines of outflows and hence the C IV blueshift becomes a diagnostic for the outflow velocity. By implication, the observed increase in C IV blueshift in the highest redshift quasars at $z \gtrsim 6$ suggests that quasar winds are potentially evolving very rapidly on time-scales of ∼200–300 Myr (Meyer et al. 2019). Thus far, the statistical studies of the rest-frame UV line properties, of quasars, have mostly focused on lower redshifts where we have samples of several hundred thousand spectra. In particular, below $z = 2.65$ the Mg II λ2800 emission line is present in the SDSS spectrum, which enables the UV line properties to be linked to black hole mass. However, in lieu of the results at the highest redshifts, it is worth extending the studies of the evolution of the rest-frame UV spectra by even a few hundred Myr while also ensuring sufficient sample statistics. We therefore focus on quasars at redshifts $3.5 < z < 4.0$ in this paper.

There are thousands of SDSS quasar spectra at $3.5 < z < 4.0$ allowing us to study the distribution of rest-frame UV line properties without the need to rely solely on sample averages. However, as accurate C IV blueshift measurements are key to this work, we also need to ensure that accurate systemic redshifts estimates are available for the full sample. At $z < 4.0$, the C III] complex is present in the SDSS observed wavelength range, which we can use to improve the systemic redshift estimates available from the SDSS pipeline, and which then allows us to measure the C IV blueshift based on the UV spectrum alone. This is crucial because while rest-frame optical emission lines or, even better, host galaxy interstellar medium lines are the gold standard for systemic redshifts, they require either near-infrared spectroscopic follow-up or Atacama Large Millimeter Array (ALMA) follow-up, which is not feasible for samples of thousands of quasars.

An additional aim of our work is to probe lower signal-to-noise SDSS spectra than what is currently analysed at $z \sim 2$. The median continuum signal-to-noise of the Rankine et al. (2020) sample is ∼6.4, compared to ∼4.9 at $3.5 < z < 4.0$. Ensuring our techniques are robust at these signal-to-noise ratios is important for the study of high-redshift quasar spectra in SDSS. At $z \gtrsim 2.7$ the SDSS wavelength coverage also means the Mg II emission line, widely used as a reliable single-epoch virial black hole mass estimator, is redshifted out of the observed spectrum, and hence we must turn to C IV for SMBH masses. A further aim of this work is to determine whether changing the SMBH mass estimator, compared to e.g. the $1.5 < z < 2.65$ samples, has an impact on the observed trends in UV line properties with SMBH mass and Eddington-scaled accretion rate (e.g. Temple et al. 2023). By measuring robust blueshifts from only the rest-frame UV spectra, and doing so at modest signal-to-noise, as well as demonstrating that the trends in these line properties are not sensitive to the SMBH mass estimator, we potentially open the door to studies of the evolution in UV line properties for much larger statistical samples out to high-redshifts e.g. those being assembled with DESI and 4MOST.

The structure of the paper is as follows. In Section 2, we present the selection of the $3.5 < z < 4.0$ sample and its subsequent post-processing. Section 3 describes the spectral reconstruction recipe used to characterize the emission line properties. Our key results are compared with the Rankine et al. (2020); Temple et al. (2023) $1.5 < z < 3.5$ samples in Section 4, before discussing their implications in the context of the redshift evolution of quasar-driven outflows in Section 5. Vacuum wavelengths are employed throughout the paper and we adopt a Lambda cold dark matter cosmology with $h_0 = 0.71$, $\Omega_M = 0.27$, and $\Omega_\Lambda = 0.73$ when calculating quantities such as quasar luminosities.

2. DATA

Our quasar sample is drawn from the final instalment of the SDSS-IV quasar catalogue, otherwise referred to as the 16th data release of the extended Baryon Oscillation Spectroscopic Survey (Dawson et al. 2016). The catalogue, which we will refer to as DR16Q, is comprised of 750 414 quasars, including the ∼526 000 known quasars from SDSS-I/II/III and a further 225 082 quasars new to SDSS catalogues (Lyke et al. 2020). We select a sample of 2775 non-Broad Absorption Line (BAL) quasars (BAL probability ≤ 0.7) in the redshift range $3.5 < z < 4.0$ from the DR16Q quasar catalogue, which have a median signal-to-noise ≥3.0 per pixel in the rest-frame interval 1265–1950 Å. Above $z > 4$, the numbers of quasars in DR16Q are relatively small precluding a statistical analysis of their UV line demographics. Furthermore, at $z > 4$, the C III] emission line complex redshifts out of the SDSS observed wavelength range, which mean systemic redshift estimates based solely on rest-frame UV spectra, become increasingly unreliable (Hewett & Wild 2010; Wu & Shen 2022). We therefore restrict our sample to $3.5 < z < 4.0$.

We follow a routine similar to that described by Hewett & Wild (2010) and later adopted by Coatman et al. (2016, 2017) and Rankine et al. (2020) to remove narrow absorption features and sky line residuals from the spectra. First, we define a 61-pixel median filtered `pseudo-continuum`. We then exclude any pixels that fall within 6 Å of the strong night-sky emission lines at 5578.5 Å and 6301.5 Å. Pixels that fall below 2σ of the `pseudo-continuum` are regarded as narrow line absorption features and hence removed from the spectrum with a grow radius of two pixels. The removed pixels are consequently replaced by their corresponding pixel in the `pseudo-continuum` spectrum.

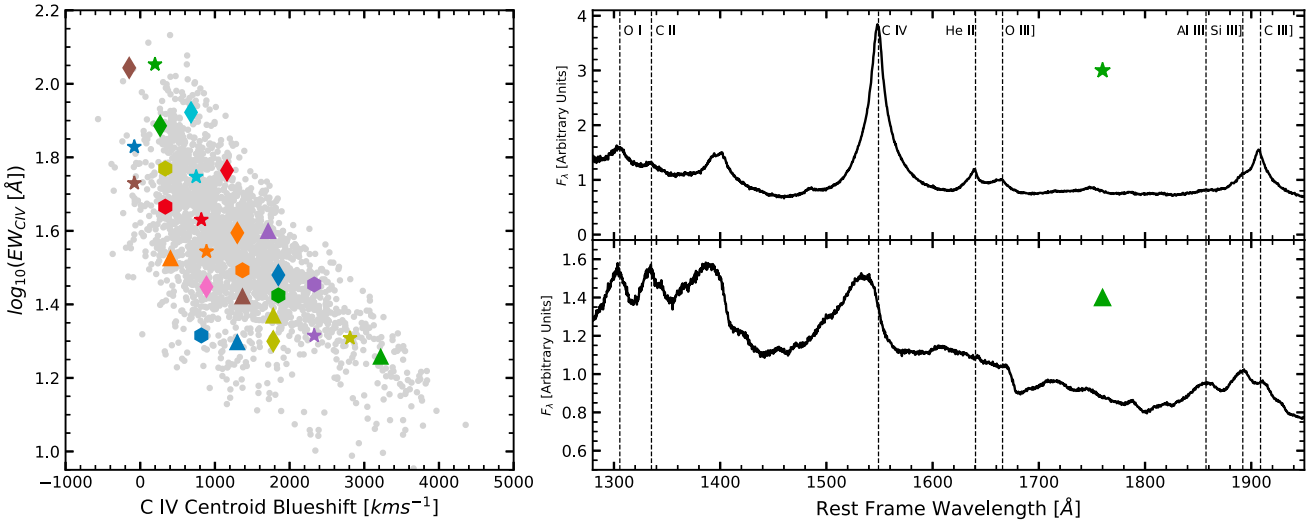

Figure 1. Left-hand panel: The left-hand panel shows the C IV blueshift versus EW for the $3.5 < z < 4.0$ quasar sample with the locations of the 33 high signal-to-noise templates used in the cross-correlation algorithm to calculate systemic redshifts. Right-hand panel: The spectra for templates at the extremes of the C IV emission space are also presented on the right-hand panel. The high C IV EW and low C IV blueshift template (top-right panel) features a strong symmetric C IV line profile. Conversely, the low C IV EW and high C IV blueshift template (bottom-right panel) features both a weak and asymmetric C IV line profile and stronger Si III] relative to C III]. Accounting for these systematic changes in the SEDs as a function of the C IV line properties is critical to producing accurate systemic redshifts.

2.1 Improving SDSS systemic redshift estimates

The accuracy to which the SDSS pipeline estimates the systemic redshift of quasars has greatly improved since DR7 (Shen et al. 2011). The DR16Q catalogue includes a number of redshift estimates for each quasar (Lyke et al. 2020) e.g. automated classifications from the SDSS spectroscopic pipeline, visual inspection estimates (which reveal that only 2.1 per cent of the automated classifications result in a catastrophic failure), and redshifts based on principal component analysis (PCA; Lyke et al. 2020). In this work, we define $Z_{\rm SDSS}$ as the 'primary' redshift presented in DR16Q, defined by either visual inspection or automated classifications. For our sample, $Z_{\rm SDSS} = Z_{\rm VI}$ for 2527 quasars and $Z_{\rm SDSS} = Z_{\rm AUTO}$ for the remaining four objects. Nevertheless, these redshift estimates do not as yet account for the systematic velocity offsets between different quasar emission lines as a function of the UV emission line morphologies. This becomes increasingly true at high redshifts, where the C IV emission line begins to dominate the redshift estimates.

Accurate systemic redshifts are crucial to our study and we therefore calculate updated systemic redshifts for our sample of high-redshift quasars as follows. A visual inspection of all 2775 ($3.5 < z < 4.0$) non-BAL quasar spectra shows that 244 quasars do not show clear broad emission line features and we therefore consider these objects to be misclassified. This number represents a larger fraction of misclassified objects than those found in among all SDSS quasar targets (Lyke et al. 2020). To improve the systemic redshift estimates, we adopt a filtering and 'cross-correlation' scheme as described in section 4.2 of Hewett & Wild (2010). There are two key differences compared to Hewett & Wild (2010). First, we employ 33 high signal-to-noise composite spectra. The composite spectra are generated using median stacks of individual SDSS quasar spectra whose systemic redshifts are calculated using the 1600–3000 Å wavelength region, including the C III] emission complex and the Mg II emission line. The 33 composite spectra span the full range of C IV emission morphologies in EW and blueshift space, as illustrated in Fig. 1. The properties of the composite spectra are summarized in Table 1. Second, the cross-correlation between each template and an individual quasar spectrum is performed with the quasar redshift as a free parameter. Finally, we create a bespoke template from the weighted mean of the seven composite spectra with the largest cross-correlation values, using the cross-correlation coefficients as the weights, and perform one last cross-correlation with the individual spectrum, again with the redshift as a free parameter.

Fig. 1 (right-hand panel) depicts two templates from the top-left and bottom-right panels of the C IV emission space shown in Fig. 1 (left-hand panel). The main difference in our approach to the estimation of systemic redshifts employing the C IV emission line is the use of templates that span the full range of emission line morphologies. The SDSS scheme employing their PCA five-components, for example, does not have the capability to reproduce the full range of quasar UV SEDs, particularly at the extremes of the CIV emission-line space. We present composite spectra for objects with systemic redshift corrections $-800 < \delta v < -600$ km s^{-1} or $600 < \delta v < 800$ km s^{-1} in Fig. 2. Fig. 2 illustrates that the systemic redshifts have dramatically improved with respect to the initial SDSS estimates. The centroids of the semiforbidden Si III]λ1892 and C III]λ1908 emission are more consistent with the rest-frame wavelengths, after a correction to the systemic redshift was applied (Fig. 2; blue). This is in contrast with the C IV emission since semiforbidden lines are produced at larger radii and should therefore not be present in outflows. We also note a similar effect in the higher energy O I]λ1306, C II]λ1335, and Si IV]λ1398 emission lines as well as the He IIλ1640 and O III] λ1665 complex.

We compare the systemic redshifts presented in DR16Q against the corrected redshifts, from this work, and find that 781 objects require systemic redshift corrections in excess of 500 km s^{-1}, 244 of which are in excess of 1000 km s^{-1}, corresponding to ∼31 per cent and ∼10 per cent of the sample, respectively.

Table 1. We present estimates of the average signal-to-noise, C IV EW and C IV blueshift for the 33 high signal-to-noise composite spectra used to correct the systemic redshifts of our sample. The signal-to-noise estimates are calculated assuming the individual spectra have a median continuum signal-to-noise ∼5. We also provide file names for the composites, which are available as online only supplementary material, in addition to the total number of spectra used to construct them. In total, 62 464 quasar spectra were used.

File name	No. of spectra	Signal-to-noise	C IV EW (Å)	C IV blueshift (km s^{-1})
mc_00000500_hew500.fits	500	110	113	197
mc_00000500_lew500p1.fits	5460	370	33.5	404
mc_00000500_lew500p2.fits	5461	370	46.3	336
mc_00000500_lew500p3.fits	5461	370	58.8	336
mc_00000500_lew500p4.fits	5459	370	76.8	266
mc_00000500_lew500.fits	500	110	21.7	404
mc_05001000_hew500.fits	500	110	83.6	680
mc_05001000_lew500p1.fits	3942	310	28.1	887
mc_05001000_lew500p2.fits	3942	310	35.0	887
mc_05001000_lew500p3.fits	3942	310	42.7	818
mc_05001000_lew500p4.fits	3942	310	55.9	749
mc_05001000_lew500.fits	500	110	20.7	818
mc_10001500_hew500.fits	500	110	58.1	1162
mc_10001500_lew500p1.fits	2402	250	26.4	1369
mc_10001500_lew500p2.fits	2403	250	31.2	1369
mc_10001500_lew500p3.fits	2403	250	39.3	1300
mc_10001500_lew500.fits	500	110	19.8	1300
mc_15002000_hew500.fits	500	110	39.8	1712
mc_15002000_lew500p1.fits	841	150	23.4	1781
mc_15002000_lew500p2.fits	840	150	26.6	1850
mc_15002000_lew500p3.fits	842	150	30.2	1850
mc_15002000_lew500.fits	500	110	19.9	1781
mc_20002500_010025.fits	799	140	20.6	2330
mc_20002500_025050.fits	674	130	28.4	2330
mc_25003000_all.fits	744	140	20.3	2809
mc_30006000_all.fits	577	120	18.1	3219
mc_m05000000_hew500.fits	500	110	111	−148
mc_m05000000_lew500p1.fits	1647	200	39.9	−78.8
mc_m05000000_lew500p2.fits	1647	200	53.7	−78.8
mc_m05000000_lew500p3.fits	1647	200	67.4	−78.8
mc_m05000000_lew500p4.fits	1647	200	80.4	−148
mc_m05000000_lew500.fits	500	110	27.1	−148
mc_m10000500_all.fits	742	140	54.9	−562

3. METHODS

3.1 Spectral reconstructions using mean field independent component analysis

An objective of our work is to compare the emission line properties of the $3.5 < z < 4.0$ quasars to lower redshift quasars at $1.5 < z < 3.5$ using exactly the same methods to analyse and fit the quasar spectra. This avoids biases in the measured line properties due to the different line-fitting procedures employed for quasars at different redshifts.

Our lower redshift comparison sample of quasars used throughout this work is drawn from Rankine et al. (2020) and Temple et al. (2023), covering the redshift range $1.5 < z < 3.5$. The rest-frame UV line demographics for quasars with $1.5 < z < 2.65$ and where the Mg II emission line is available for robust SMBH mass measurements, has been studied in detail by Temple et al. (2023). Analogous to Rankine et al. (2020) we therefore employ a technique called mean-field independent component analysis (MFICA; Højen-Sørensen, Winther & Hansen 2002) to provide essentially noise-free reconstructions of each observed spectrum through a linear combination of 7–10 component spectra (see section 4.2 of Rankine et al. 2020 for more details). The component spectra are the same as those used by Rankine et al. (2020) at $1.5 < z < 3.5$. They were generated using a sample of ∼4000 ($1.5 < z < 3.5$) spectra at intermediate C IV EWs, 20–40 Å, and a further two samples of ∼2000 ($1.5 < z < 3.5$) spectra with C IV EW >40 Å and <20 Å. The scheme for deriving MFICA-components for use on astronomical data is described in Allen et al. (2013). Three sets of components were necessary to account for the extensive array of C IV emission line morphologies seen in the sample. For a visualization of the three sets of MFICA components, which will be made available as online only supplementary material, see Appendix A. The MFICA components are highly effective for our purpose; however, the exact form of the components is not important. Rather, the key requirement is that the components can be combined to produce accurate reconstructions of the quasar spectra. Alternative approaches using PCA or non-negative matrix factorization should also work well.

Spectrophotometric calibration effects introduce both a blue excess and red decrement to the BOSS spectra (Dawson et al. 2012; Pâris et al. 2012). Consequently, we observe an ∼ ±10 per cent multiplicative factor in the spectrophotometry as well as an additional effect introduced by the varying dust extinction towards each quasar. Since we aim to reconstruct the quasar spectra with linear combinations of fixed components, any wavelength-dependent multiplicative factor needs to be removed, hence we implement a 'morphing' recipe to standardize the shape of the quasar spectra. For a full description

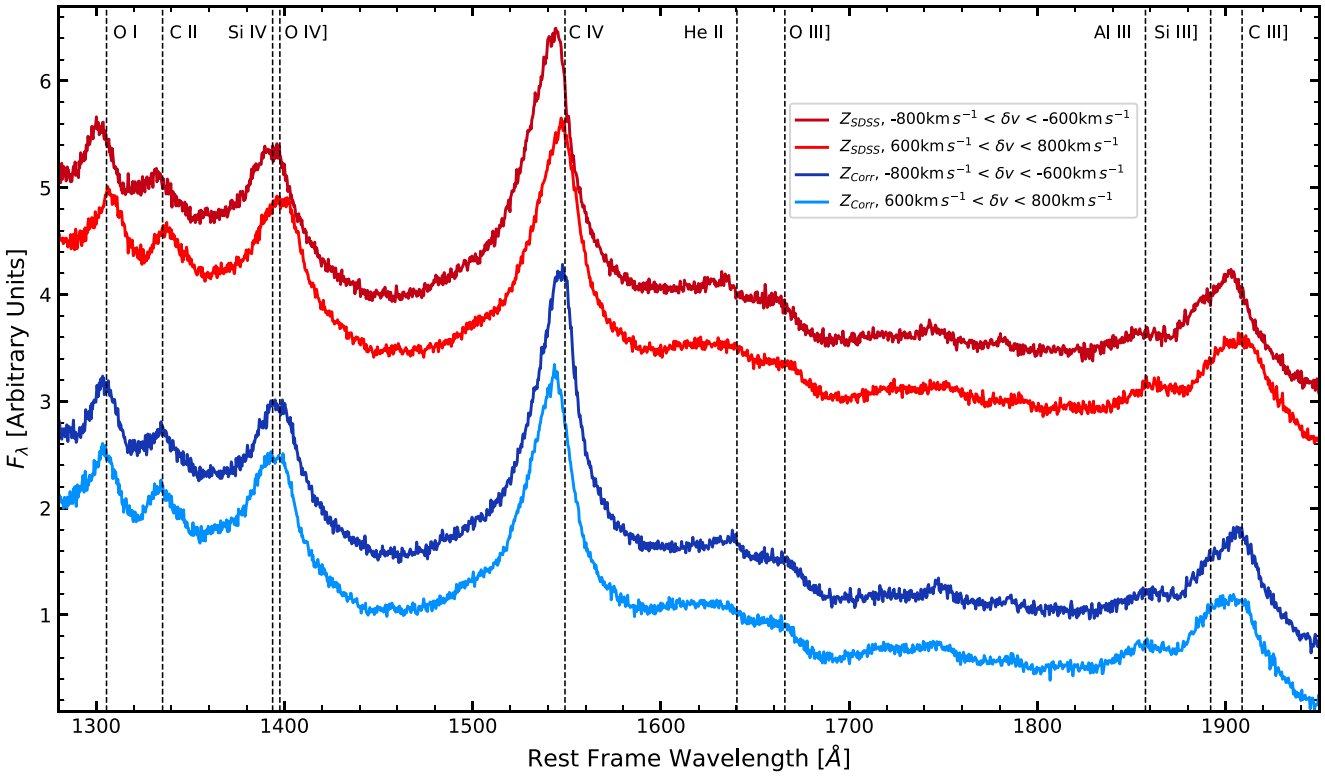

Figure 2. Composites of quasar spectra with redshift corrections $-800 < \delta v < -600$ km s^{-1} or $600 < \delta v < 800$ km s^{-1}. We present composites before a redshift correction is applied (red) and afterwards (blue). The corrected composites (blue) align with the lower ionization lines, such as O I, C II, Si IV], and O IV far more convincingly than when the original SDSS systemic redshifts are used.

of the morphing recipe see section 4.1 of Rankine et al. (2020). The reference quasar SED used to 'morph' the quasar spectra is a model quasar spectrum, discussed extensively in Maddox et al. (2012) and Temple, Hewett & Banerji (2021).[1]

We use the EMCEE Python package[2] (Foreman-Mackey et al. 2013) for the MFICA spectral reconstructions. The EMCEE package is a Python implementation of the affine-invariant ensemble sampler for Markov-chain Monte Carlo (MCMC) simulations, proposed by Goodman & Weare (2010). We permit the EMCEE package to explore an N-dimensional, Gaussian likelihood function, where N represents the number of MFICA components ($N = 7$ for the high C IV EW set and $N = 10$ otherwise), and apply uniform priors to the component weights. Example spectra, with various signal-to-noise characteristics are presented in Fig. 3 together with their MFICA reconstructions. A key conclusion is that the $1.5 < z < 3.5$ MFICA components can successfully reconstruct the $3.5 < z < 4.0$ spectra with a range of signal-to-noise ratios. The MFICA has the effect of boosting the signal-to-noise characteristics of the SDSS spectra affording us the opportunity to analyse weaker UV emission lines such as He II. We have checked that different realizations of the spectra perturbed consistent with the Gaussian noise on each spectrum, result in essentially identical MFICA reconstructions. Although the component weights themselves change, the line properties derived from the reconstructions are therefore unchanged by the noise on each spectrum. A further advantage of MFICA over parametric fitting of emission lines is the ability to accurately reproduce asymmetric emission line features. For a full discussion, and comparison to catalogues where line properties are determined via parametric fitting, refer to Appendix B.

[1] https://github.com/MJTemple/qsogen
[2] https://github.com/dfm/emcee

3.2 Line properties

A central aim of this work is to assess whether there is any redshift evolution in the rest-frame UV emission line properties from $1.5 < z < 4.0$. To determine the C IV EW and blueshift, we first define a power-law continuum, $f(\lambda) \propto \lambda^{-\alpha}$. We then follow the non-parametric approach discussed by Coatman et al. (2016, 2017), whereby the median values of F_λ in the two wavelength regions 1445–1465 Å and 1700–1705 Å are used to determine the power-law approximation. Then, C IV EW measurements are made via numerical integration. Due to the well-known asymmetry of the C IV emission line (Richards et al. 2011), we define the blueshifts as the difference between the line centroid and rest-frame wavelength:

$$\text{C IV blueshift} = c(\lambda_r - \lambda_{\text{half}})/\lambda_r \ \ [\text{km s}^{-1}] \quad (1)$$

where c is the velocity of light, λ_{half} is the rest-frame wavelength of the flux-weighted line centroid, and λ_r is 1549.48 Å for the C IV doublet. We note that several papers in the literature exploring the UV emission line properties of high-redshift quasars (e.g. Meyer et al. 2019; Schindler et al. 2020) use the observed wavelength corresponding to the peak of the line to define the C IV blueshift. This is often necessary at low signal-to-noise but does not fully capture the often significant flux in the blue wing of the C IV emission line.

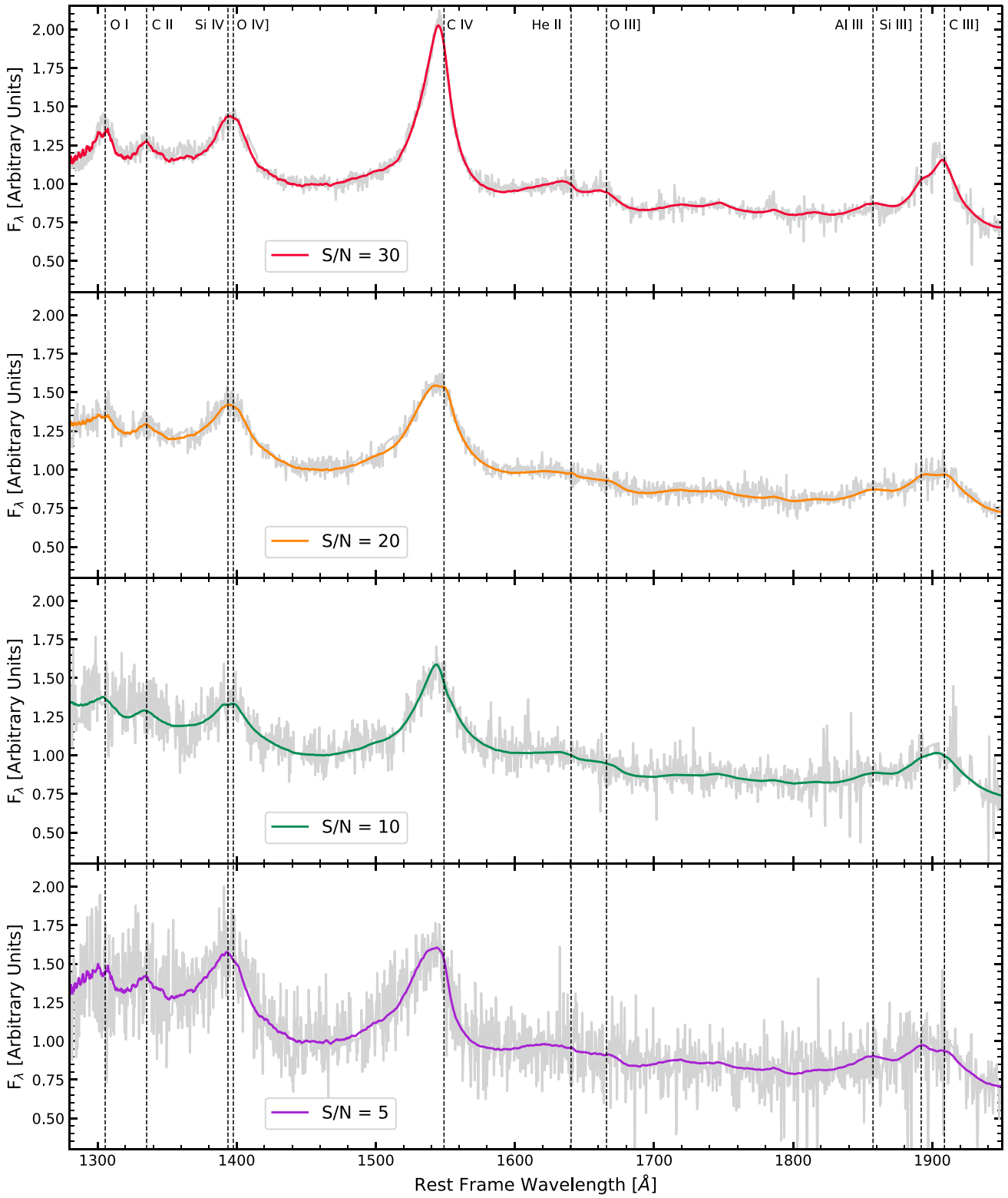

Figure 3. Example quasar spectra from our sample at $3.5 < z < 4.0$ with signal-to-noise of 30 (top panel), 20 (top-middle panel), 10 (bottom-middle panel), and 5 (bottom panel), with their corresponding MFICA reconstructions overlaid. We can see that the MFICA reconstructions have the effect of boosting the signal-to-noise of the SDSS spectra, and hence robust UV emission line analysis becomes achievable.

Table 2. The format of the table containing the emission line properties from our MFICA reconstructions. The table is available in a machine-readable format in the online journal.

Header	Units	Description
SPEC_FILE	—	SDSS spec file name
RA	Degrees	Right ascension
DEC	Degrees	Declination
REDSHIFT	(—, —, km s^{-1})	$Z_{\rm SDSS}$, $Z_{\rm Corrected}$, and velocity shift
LOG_L1350	$\log_{10}$(erg s^{-1})	Monochromatic continuum luminosity at 1350 Å
LOG_L3000	$\log_{10}$(erg s^{-1})	Monochromatic continuum luminosity at 3000 Å
LOG_MBH_CIV_COATMAN	$\log_{10}$(M$_\odot$)	C IV derived $M_{\rm BH}$[a]
LOG_LAMBDA_EDD	—	Eddington-scaled accretion rate
C_IV	(Å, km s^{-1}, km s^{-1}, km s^{-1})	C IV: EW, centroid blueshift, FWHM, and $FWHM_{\rm Coat,Corr}$[a]
HE_II	Å	He II: EW

Note.
[a]The C IV FWHM Coatman et al. (2017) correction has been applied.

3.3 Luminosities and black hole masses

We infer rest-frame monochromatic continuum luminosities λL_λ at $\lambda = 3000$ and 1350 Å (hereafter L_{3000} and L_{1350}, respectively) using the point spread function magnitudes from SDSS photometry reported in the Lyke et al. (2020) DR16Q catalogue. The SDSS photometry is corrected for Galactic dust extinction using the reddening law presented by Schlafly & Finkbeiner (2011) and the quasar-specific pass-band attenuations described in section 3.1.4 of Temple et al. (2021). For each object, we then fit a quasar SED model (Temple et al. 2021) to the extinction-corrected photometry using the improved spectroscopic redshifts described in Section 2.1, with the quasar luminosity and continuum reddening $E(B-V)$ as the only free parameters. The $E(B-V)$ accounts for the (slight) variations observed in UV continuum slope and allows a robust estimation of the rest-frame L_{3000}, which in turn allows us to estimate bolometric luminosities in the same way for our $z > 3.5$ and $z \approx 2$ samples. We exclude pass-bands with rest-frame wavelengths $\lambda < 1215$ Å, which results in the use of data from the *riz* pass-bands for our $z > 3.5$ sample, and the *griz* pass-bands for our $1.5 < z < 2.65$ comparison sample from Rankine et al. (2020).

As the Mg II λ2800 emission line is absent from SDSS spectra at redshifts $z \gtrapprox 2.7$, we estimate SMBH masses for our $3.5 < z < 4.0$ sample using the full width at half-maximum (FWHM) of the C IV emission. Due to the asymmetric wing, bluewards of the C IV peak emission, we apply a correction to the $(\mathrm{FWHM})_{\rm C\,IV}$ derived from the correlation between the FWHM of the C IV and H_β emission lines – see equation 5 and section 4.3 of Coatman et al. (2017) for further details.

$$(\mathrm{FWHM})_{\rm C\,IV,Corr.} = \frac{(\mathrm{FWHM})_{\rm C\,IV}}{(0.36 \pm 0.03)\left(\frac{\rm C\,IV\ blueshift}{10^3\ \rm km\,s^{-1}}\right) + (0.61 \pm 0.04)} \quad (2)$$

The functional form of equation (2) leads to inappropriate mass estimates for objects with modest (or indeed negative) blueshifts, hence we only apply the correction on those objects whose C IV blueshift is >500 km s^{-1} (fig. 6; Coatman et al. 2017). We correct the $(\mathrm{FWHM})_{\rm C\,IV}$ under the assumption that the C IV blueshift = 500 km s^{-1}, for the quasars that fall short of this threshold although the results would be qualitatively unchanged if no correction was applied to quasars with blueshifts of < 500 km s^{-1}. The mass estimates are then calculated using equation (3):

$$(\mathrm{M_{bh}})_{\rm C\,IV,Corr.} = 10^{6.71}\left(\frac{(\mathrm{FWHM})_{\rm C\,IV,Corr.}}{10^3\ \rm km\,s^{-1}}\right)^2\left(\frac{\lambda \mathrm{L}_\lambda(1350A)}{10^{44}\ \rm erg\,s^{-1}}\right)^{0.53}. \quad (3)$$

To determine the Eddington-scaled accretion rates of our sample, we use the 3000 Å rest-frame luminosities and C IV derived SMBH masses. We apply the bolometric correction $BC_{3000} = 5.15$ (Shen et al. 2011; Rankine et al. 2020) to convert the 3000 Å rest-frame luminosities to bolometric luminosities from which we can calculate the Eddington-scaled accretion rates for our sample. A catalogue of all line properties derived from these spectra will be available as online only supplementary material. Details of the catalogue are presented in Table 2.

4. RESULTS

In this section we present the C IV and He II line properties for the $3.5 < z < 4.0$ quasar sample and compare to quasars at $1.5 < z < 3.5$ from the literature.

4.1 C IV emission

Fig. 4 shows the distribution of the C IV blueshifts and EWs in the $3.5 < z < 4.0$ sample as well as the $1.5 < z < 3.5$ sample from Rankine et al. (2020) and Temple et al. (2023). The Rankine et al. (2020) sample utilizes SDSS DR14 so we supplement the sample with a small number of additional quasars in the same redshift range from DR16Q. Consistent with the findings of Richards et al. (2011), Coatman et al. (2016, 2017), and Rankine et al. (2020), we observe an anticorrelation between the C IV blueshift and C IV EW of the emission lines. Stronger emission lines are generally symmetric and show modest C IV blueshifts while weaker lines exhibit a range of blueshifts with a clear tail extending to very high blueshifts of several thousands of kilometre per second. While we find that both the $1.5 < z < 3.5$ and $3.5 < z < 4.0$ samples have the same characteristic distribution in the C IV emission space, as expected, the $3.5 < z < 4.0$ objects do not populate the same region as the $1.5 < z < 3.5$ sample. Due to the well-known Baldwin effect, the more luminous $3.5 < z < 4.0$ quasars are biased towards lower C IV EWs and the $3.5 < z < 4.0$ quasars also show a tail extending to much higher C IV blueshifts.

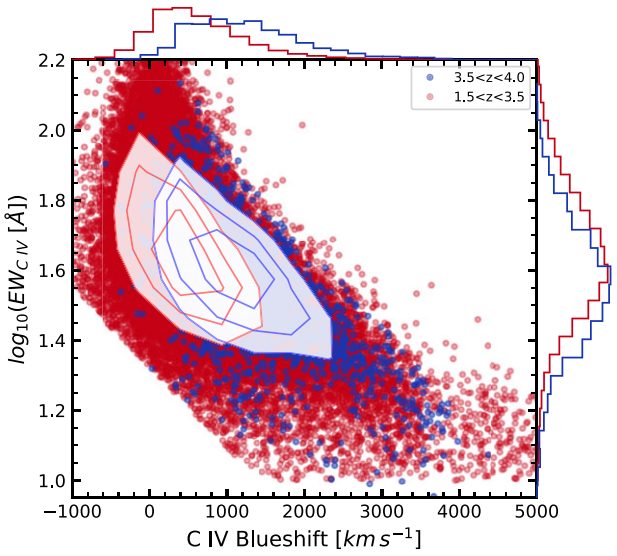

Figure 4. The C IV emission space for both the $1.5 < z < 3.5$ (red, Rankine et al. 2020; Temple et al. 2023) and $3.5 < z < 4.0$ (blue) samples. Density contours encircle 68 per cent, 50 per cent, and 25 per cent of the sample, respectively. Marginalized distributions of the C IV blueshift and EW are also shown. While the distributions feature the same characteristic shape, the $3.5 < z < 4.0$ sample is biased to higher C IV blueshift and lower C IV EW. The following criterion was applied to remove poorly fit spectra from both samples; $\log_{10}$(C IV EW [Å]) $< -2.3077 \times 10^{-4} \times$ C IV blueshift [km s^{-1}] + 1.3231.

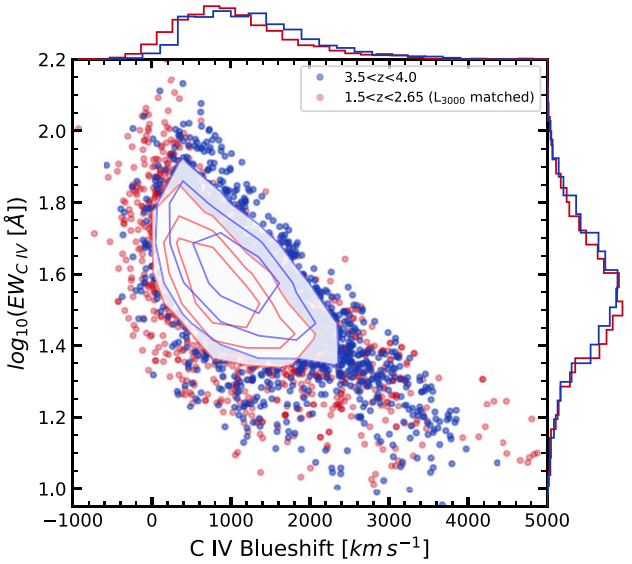

Figure 5. The C IV emission space for the $3.5 < z < 4.0$ sample (blue) and the L_{3000} matched $1.5 < z < 2.65$ quasars (red) from Temple et al. (2023). Density contours encircle 68 per cent, 50 per cent, and 25 per cent of the sample, respectively.

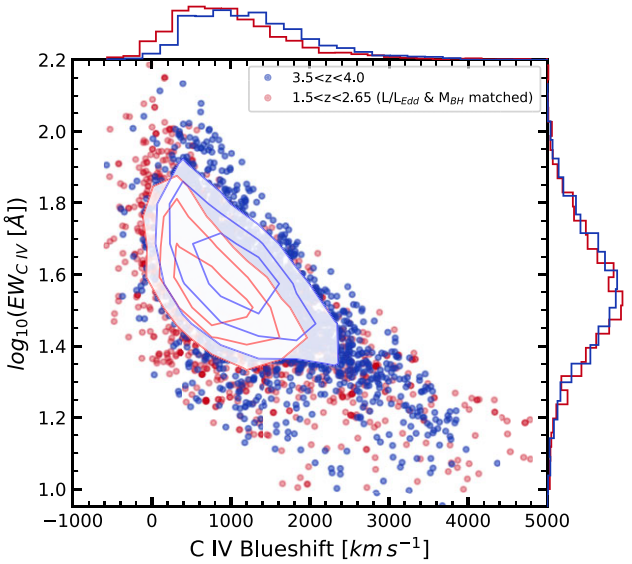

Figure 6. The C IV emission space for the $3.5 < z < 4.0$ sample (blue) and the $M_{\rm BH}$ and $L/L_{\rm Edd}$ matched $1.5 < z < 2.65$ quasars (red) from Temple et al. (2023). Density contours encircle 68 per cent, 50 per cent, and 25 per cent of the sample, respectively.

4.1.1 *Matching the samples by quasar properties*

To ensure a fair comparison between $3.5 < z < 4.0$ and cosmic noon, we match our $3.5 < z < 4.0$ quasars to the $1.5 < z < 2.65$ DR16Q sample from Temple et al. (2023), by choosing the nearest $1.5 < z < 2.65$ quasar to each $3.5 < z < 4.0$ quasar in a variety of quasar physical properties. Specifically we match in turn by 3000 Å continuum luminosity and *both* SMBH mass and Eddington-scaled accretion rate. For the lower redshift sample the SMBH masses are derived from the Mg II emission line, while at higher redshifts of $z > 2.65$ they are derived instead using C IV. A key aim of this work is to investigate how changing the SMBH mass estimator potentially affects the dependence of UV line properties on SMBH mass and accretion rate.

We observe good agreement in the C IV emission line properties when matching the $3.5 < z < 4.0$ sample to the $1.5 < z < 2.65$ quasars in L_{3000} or both $M_{\rm BH}$ and $L/L_{\rm Edd}$. The distributions are illustrated in Figs 5 and 6, respectively. In both cases, the marginalized distributions in C IV EW are in good agreement between $1.5 < z < 2.65$ and $3.5 < z < 4.0$. The high C IV blueshift tail of the $3.5 < z < 4.0$ sample is much more consistent with the $1.5 < z < 2.65$ quasars when matching in either L_{3000} or *both* $M_{\rm BH}$ and $L/L_{\rm Edd}$, compared to the marginalized distributions presented in Fig. 4. However, the number of objects with C IV blueshift ≤ 500 km s^{-1} tails off more rapidly at $3.5 < z < 4.0$. In Appendix C, we demonstrate that this can be attributed to the reduced rest-frame wavelength coverage of the $3.5 < z < 4.0$ spectra compared to the $1.5 < z < 2.65$ spectra for systemic redshift estimation. Truncating the $1.5 < z < 2.65$ spectra to the same rest-frame wavelength range as our $3.5 < z < 4.0$ spectra (namely $\lambda < 2000$ Å) results in a slight overestimation of $z_{\rm sys}$ at lower C IV blueshifts. At these rest-frame wavelengths, we no longer have access to the Mg II λ2800 emission line for calculation of $z_{\rm sys}$. Mg II is not affected by narrow associated absorption, which can affect the C IV line profile as discussed in detail in Appendix C. This explains the discrepancies observed in the one-dimensional marginalized C IV blueshift histograms presented in both Figs 5 and 6. The high blueshift end is not affected by the systemic redshift bias due to the reduced rest-frame wavelength coverage of the high-redshift quasar spectra.

While the C IV emission line properties appear to be consistent across the entire redshift range investigated, it is important to note that the SMBH mass estimates at $1.5 < z < 2.65$ were derived from the Mg II emission line (Temple et al. 2023). As discussed in

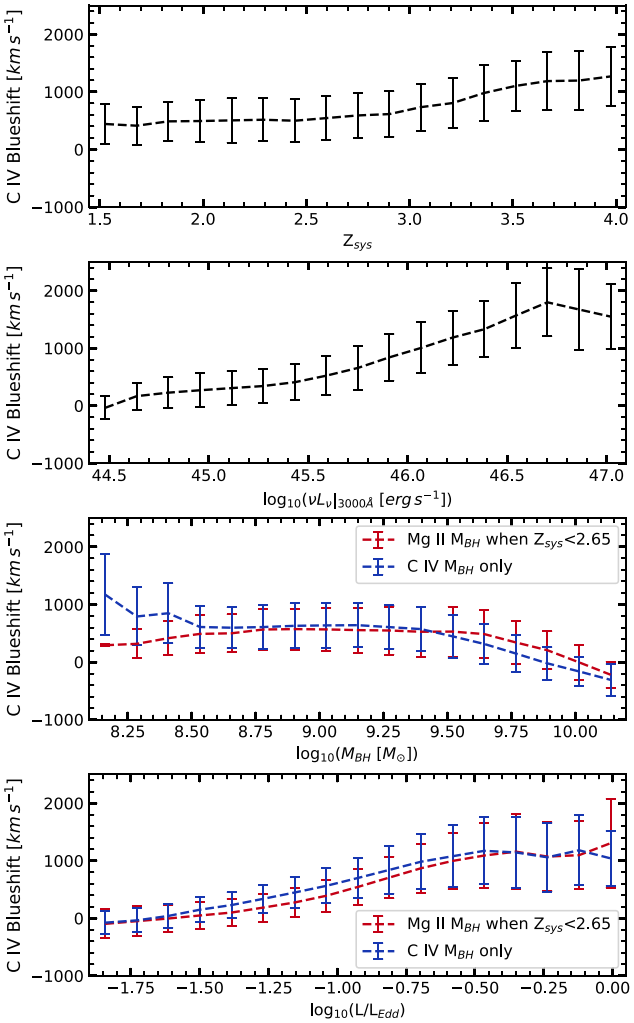

Figure 7. The C IV blueshift as a function of systemic redshift (top panel), UV continuum luminosity (top-middle panel), SMBH mass (bottom-middle panel), and Eddington-scaled accretion rate (bottom panel). The data are compressed into 17 equidistant bins, where we present the median and median absolute deviation (MAD) of each bin in the appropriate panels. We see a tendency for increasing C IV blueshifts with increasing systemic redshift, UV continuum luminosity, and Eddington-scaled accretion rate. The trends with UV continuum luminosity and Eddington-scaled accretion rate can explain why we observe an increase in C IV blueshift as we tend to larger systemic redshifts. There is limited evidence of a strong trend between SMBH mass and C IV blueshift (bottom-middle panel), with a slight tendency to lower C IV blueshifts as we approach the upper limit of our SMBH masses for the sample. There is limited evidence to suggest that the emission line used to estimate virial black hole masses will have any significant impact on our results.

Section 3.3, the SMBH masses for the $3.5 < z < 4.0$ sample are derived from the C IV emission with an associated correction to the FWHM to account for the line asymmetry (Coatman et al. 2017). This could potentially lead to biases in the results presented in Fig. 6.

In Fig. 7, we investigate how the C IV blueshift evolves with redshift, luminosity, black hole mass, and accretion rate. The C IV blueshift increases with systemic redshift (top panel). However, when one accounts for the trends in blueshift with UV luminosity (top-middle panel) and Eddington-scaled accretion rate (bottom panel), this trend can be explained by the higher luminosities probed at high redshifts due to the flux limits of the SDSS. Furthermore, when one

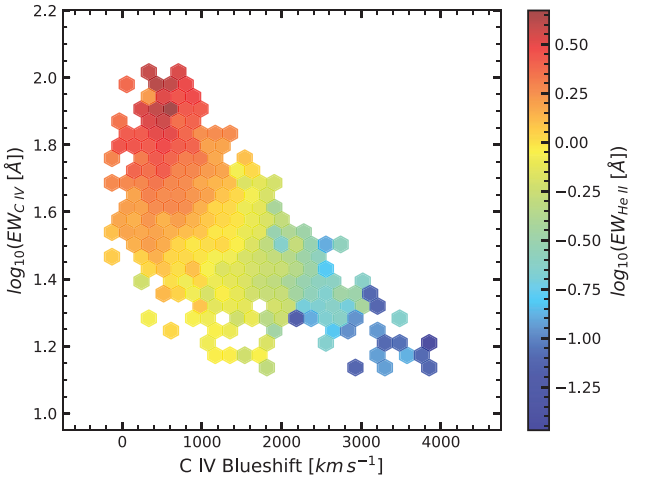

Figure 8. The median observed He II EW in bins of C IV blueshift and C IV EW for the $3.5 < z < 4.0$ sample. The He II EW is correlated with both C IV blueshift and C IV EW, with the most blueshifted C IV lines only observed when the He II EW is low. Conversely, the highest EW C IV lines are only observed when the He II EW is high.

considers the redshift evolution of the quasar luminosity function, whereby the number density of the brightest quasars exponentially decreases beyond $z \gtrsim 3.5$ (Fig. 7; Kulkarni, Worseck & Hennawi 2019), the increase in C IV blueshift at $z \sim 3$–3.5 (top panel) is consistent with the fact that we only see the most luminous quasars at these redshifts in a flux-limited sample. We also observe limited evolution in the C IV blueshift as a function of SMBH mass (bottom-middle panel) with a slight tendency for C IV blueshifts to decrease with increasing SMBH masses. In addition, we observe no significant change to the trends in Fig. 7, when we measure the black hole masses from the Mg II emission versus the C IV emission line with a blueshift dependent correction applied to the C IV FWHM (section 3; Coatman et al. 2017).

4.2 He II emission

The He II line is generated by the direct recombination of He III ions to He II (with some covering factor dependence) and is therefore a 'clean' measurement of the number of photons above 54.4 eV (section 2c; Mathews & Ferland 1987). Hence, provided that the He II line properties can be robustly measured, the He II emission is a better indicator of the ionization potential of the soft X-ray photons than C IV (Timlin, Brandt & Laor 2021; Temple et al. 2023). Through use of MFICA, we have been able to reconstruct the He II emission line profile even at relatively modest signal-to-noise ratios (see Fig. 3 and Appendix B). Fig. 8 illustrates how the He II line properties change across the C IV emission space. We recover the same trends as those uncovered by Baskin et al. (2013) and Rankine et al. (2020) at lower redshifts. Fig. 8 illustrates a clear anticorrelation between the He II EW and the C IV blueshift as well as an additional correlation between the He II and C IV EWs. We find that the same trends in He II EW and both C IV EW and blueshift are recovered when one constructs composite stacked spectra, from 20 different regions in the C IV emission space, and measures the line properties from the high signal-to-noise composites directly rather than using MFICA reconstructions. This confirms that despite the modest signal-to-noise of many of the individual spectra in the $3.5 < z < 4.0$ sample, the MFICA is still able to recover meaningful signal from the low EW emission lines.

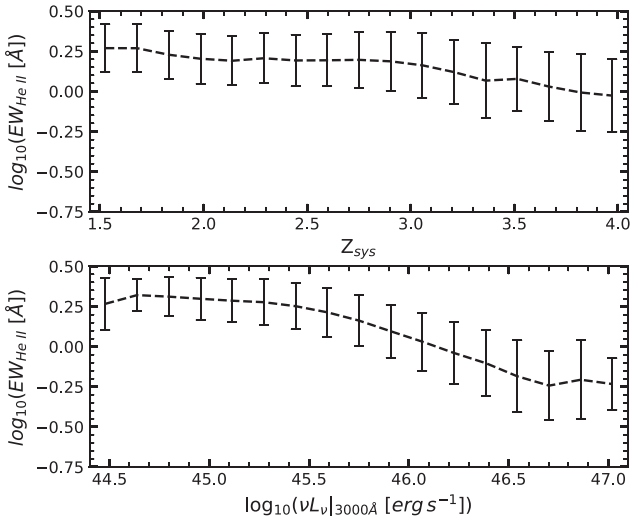

Figure 9. The He II EW as a function of systemic redshift (top panel) and UV continuum luminosity (bottom panel). The data are compressed into 17 equidistant bins, where we present the median and MAD of each bin in the appropriate panels. We see a slight tendency for decreasing He II EWs with increasing systemic redshift. The trends with He II EW and UV continuum luminosity can therefore well explain the apparent evolution with systemic redshift.

Under the assumption that the He II EW is a good proxy for the ionizing flux at 54.4 eV (see Section 5.1 for full discussion), this result is consistent with the hypothesis that UV line-driven outflows give rise to the blueshift observed in the C IV emission of quasars. A soft SED is a prerequisite for the strong blueshifting observed in the C IV emission and overionization of the outflowing material leads to weaker C IV blueshifts. In Fig. 9, we present the evolution of the He II EW as a function of both systemic redshift and UV continuum luminosity. We observe no convincing evidence of an evolution in the He II EW with systemic redshift, save for a slight tendency to lower He II EW at $3.5 < z < 4.0$. However, this tendency is well accounted for when one considers the trend in He II EW with UV continuum luminosity, whereby the He II EW decreases with luminosity and therefore with systemic redshift as a result of the sampling bias at $z \gtrsim 3.5$. Since the relation presented in Fig. 8 is observed in quasars across the entire redshift range, $1.5 < z < 4.0$, and the He II EW demonstrates little to no evolution with systemic redshift in Fig. 9, we can conclude that the SED properties of quasars remain consistent across the entire $1.5 < z < 4.0$ redshift range.

5 DISCUSSION

5.1 Probing the driver of outflows

We have explored trends in the rest-frame UV emission line properties of quasars at $1.5 < z < 4.0$, analysed using the same methodology across the full redshift range. As shown in Figs 5 and 6, we find that the C IV emission line properties, and in particular the high-blueshift tail at $3.5 < z < 4.0$ and $1.5 < z < 2.65$ are best matched when matching the quasar samples in either UV luminosity or equivalently *both* SMBH mass and Eddington-scaled accretion rate. In Fig. 8, we demonstrated that there is a strong and systematic trend between the C IV blueshift and the He II EW in $3.5 < z < 4.0$ quasars, which is qualitatively very similar to the trend found in the $1.5 < z < 3.5$ population by e.g. Rankine et al. (2020). The result is broadly consistent with a paradigm where the C IV blueshift is tracing a radiation line-driven wind with the ability to launch a wind anticorrelating with the number of high-energy ionizing photons above 54eV (Baskin et al. 2015). We will therefore proceed from hereon under the assumption that the C IV emission line properties encode information about the strength of a radiation line-driven wind. A key question of interest is how the wind properties then relate to fundamental properties of the quasar such as UV luminosity, SMBH mass, and Eddington-scaled accretion rate. Recently, Temple et al. (2023) have looked at this exact question using a sample of ∼190 000 SDSS quasars at $1.5 < z < 2.65$. We can therefore extend the Temple et al. (2023) analysis to explicitly ask if the same fundamental properties drive trends in quasar UV emission line properties at $3.5 < z < 4.0$.

Fig. 10 illustrates the $M_{\rm BH}$–$L/L_{\rm Edd}$ plane, for both the $1.5 < z < 2.65$ and $3.5 < z < 4.0$ samples, with trends in C IV blueshift, C IV EW, and He II EW at $3.5 < z < 4.0$ overlaid. As expected, we observe a clustering at $3.5 < z < 4.0$ in the top-right corner of the parameter space and the $3.5 < z < 4.0$ sample is biased to higher black hole masses and Eddington-scaled accretion rates compared to $1.5 < z < 2.65$, due to the flux limits of the SDSS survey. Crucially though, and in contrast to quasars at even higher redshifts as we discuss later, the $3.5 < z < 4.0$ sample overlaps considerably with the $1.5 < z < 2.65$ sample in SMBH mass and Eddington-scaled accretion rate.

As is the case in the $1.5 < z < 2.65$ sample, we observe the strongest outflows above $L/L_{\rm Edd} \geq 0.2$ and $M_{\rm BH} \geq 10^9$ M$_\odot$. Indeed, the trends in C IV blueshift, C IV EW, and He II EW are consistent with the $1.5 < z < 2.65$ sample results, presented in Temple et al. (2023), suggesting that the underlying drivers of these UV line properties do not evolve with redshift. We also investigate trends in the $M_{\rm BH}$–L_{3000} plane in Fig. 11. The flux limit of the $3.5 < z < 4.0$ sample is evident at $\nu L\nu|_{3000\text{Å}} \sim 45.5$ erg s^{-1}, the threshold above which quasar feedback is considered to be effective (Zakamska & Greene 2014). The trends in line properties in the $M_{\rm BH}$–L_{3000} plane are also consistent with those seen in $1.5 < z < 2.65$ quasars by Temple et al. (2023). A key result of our work is therefore explicitly demonstrating that redshift is not a fundamental parameter in determining quasar UV emission line (and by implication outflow) properties and that these properties are instead governed by SMBH mass and accretion rate. Moreover, the results are not sensitive to the emission line used for the SMBH mass estimates, which demonstrates that with large enough statistical samples global trends of UV line properties with SMBH mass and accretion rate can be recovered even when one uses C IV lines for SMBH mass estimates (e.g. Fig. 7).

Giustini & Proga (2019) have proposed that accreting black holes with a mass, $M_{\rm BH} \geq 10^8$ M$_\odot$, and an Eddington-scaled accretion rate, $L/L_{\rm Edd} \geq 0.25$ are expected to facilitate strong radiation-driven winds. Conversely, objects whose Eddington-scaled accretion rate falls below this threshold will likely produce failed line-driven disc winds, or in extreme cases, the outflowing material is magnetically driven, and the feedback kinetic. Temple et al. (2023) find that the observations at $1.5 < z < 2.65$ are in good agreement with the proposed framework, only measuring significant C IV blueshifts (≥ 1000 km s^{-1}), at $1.5 < z < 2.65$, when objects are both strongly accreting and high mass. We confirm that at $3.5 < z < 4.0$, the C IV blueshift is again strongly dependent on the mass and accretion rate in much the same way as for the $1.5 < z < 2.65$ population and that at high accretion rates and lower SMBH masses, the ionizing potential above 54.4 eV, as traced by the He II EW, prevents strong disc winds from being launched.

Fundamentally, the similarity in the trends in UV emission line properties with luminosity, mass, and accretion rate between $1.5 < z < 2.65$ and $3.5 < z < 4.0$, strongly suggests that the same

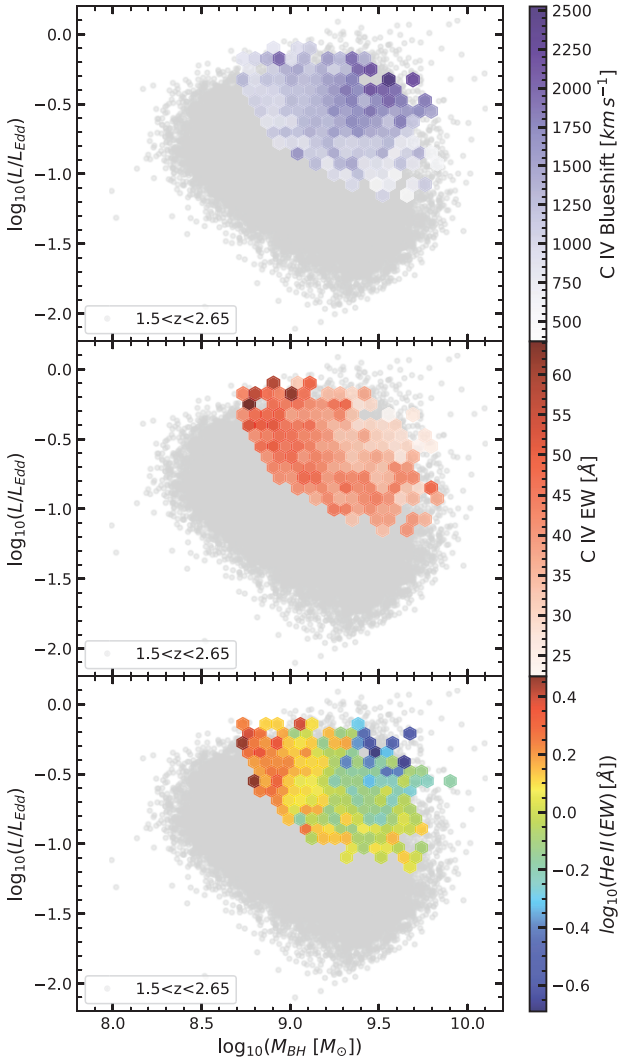

Figure 10. The median observed C IV blueshift (top panel), C IV EW (middle panel), and He II EW (bottom panel) in bins of SMBH mass and Eddington-scaled accretion rate for the $3.5 < z < 4.0$ sample overlaid on the $M_{\rm BH}$–$L/L_{\rm Edd}$ plane at $1.5 < z < 2.65$ (grey, Temple et al. 2023). Save for a clear flux limit, the $1.5 < z < 2.65$ and $3.5 < z < 4.0$ samples are well-matched in this space. We note that above $L/L_{\rm Edd} \sim 0.2$ there is evidence of a clear trend between He II EW and SMBH mass. Below $\sim 10^9$ $M_\odot$, the quasars generally have stronger UV emission lines and weaker C IV blueshifts and above this threshold, the contrary is true.

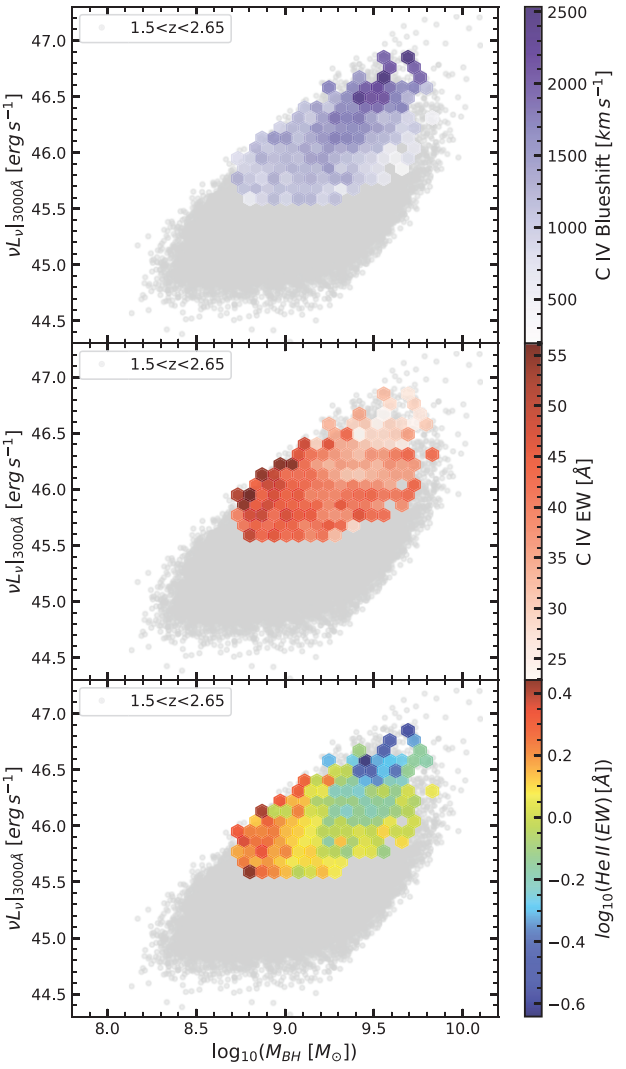

Figure 11. The median observed C IV blueshift (top panel), C IV EW (middle panel), and He II EW (bottom panel) in bins of SMBH mass and 3000 Å UV continuum luminosity for the $3.5 < z < 4.0$ sample overlaid on the $M_{\rm BH}$–L_{3000} plane at $1.5 < z < 2.65$ (grey, Temple et al. 2023). A clear flux limit is observed at $\nu L\nu|_{3000\text{Å}} \sim 45.5$ erg s^{-1} in the $3.5 < z < 4.0$ sample. Apart from that the $1.5 < z < 2.65$ and $3.5 < z < 4.0$ samples are well-matched in this space. Below $\sim 10^9$ $M_\odot$, the quasars have stronger UV emission lines and smaller C IV blueshifts. Above this threshold, the contrary is true.

accretion and wind-driving mechanisms are at play across the entire $1.5 < z < 4.0$ redshift range. We will now discuss the implication of these results for studies of quasar winds and outflows at even higher redshifts, where there have been claims that the UV emission line properties do indeed show some evolution (Meyer et al. 2019; Schindler et al. 2020; Yang et al. 2021; Farina et al. 2022).

5.2 Implications at higher redshifts

Previous studies of quasars at the highest redshifts of $z \gtrsim 6$ have concluded that their emission line properties, and in particular C IV blueshifts are on average higher than quasars at lower redshifts even when the samples are matched in UV luminosity. We now consider quasar samples at $z \sim 4.8$ from Trakhtenbrot et al. (2011) and at $z \gtrsim 6$ from Schindler et al. (2020) for explicit comparison to our work. As has been done in the literature, we construct a control sample of $1.5 < z < 2.65$ quasars drawing from the sample in Temple et al. (2023), and matching to the high-redshift samples in UV luminosity. In Fig. 5, we found that matching the $3.5 < z < 4.0$ and $1.5 < z < 2.65$ samples in UV luminosity resulted in a good agreement in the C IV emission properties. The left-hand panel of Fig. 12 illustrates that the UV luminosity matching across the two redshift bins, results in a broadly consistent mapping to the $M_{\rm BH}$–$L/L_{\rm Edd}$ plane, which we have already determined in Section 5.1 are the fundamental parameters driving trends in C IV blueshift. However, when we consider the Trakhtenbrot et al. (2011) and Schindler et al. (2020) quasars at $z \sim 5$–7, the UV-luminosity matched control samples no longer map on to the same region of the $M_{\rm BH}$–$L/L_{\rm Edd}$ plane as the high-redshift quasars, as illustrated in the right-hand panel of Fig. 12.

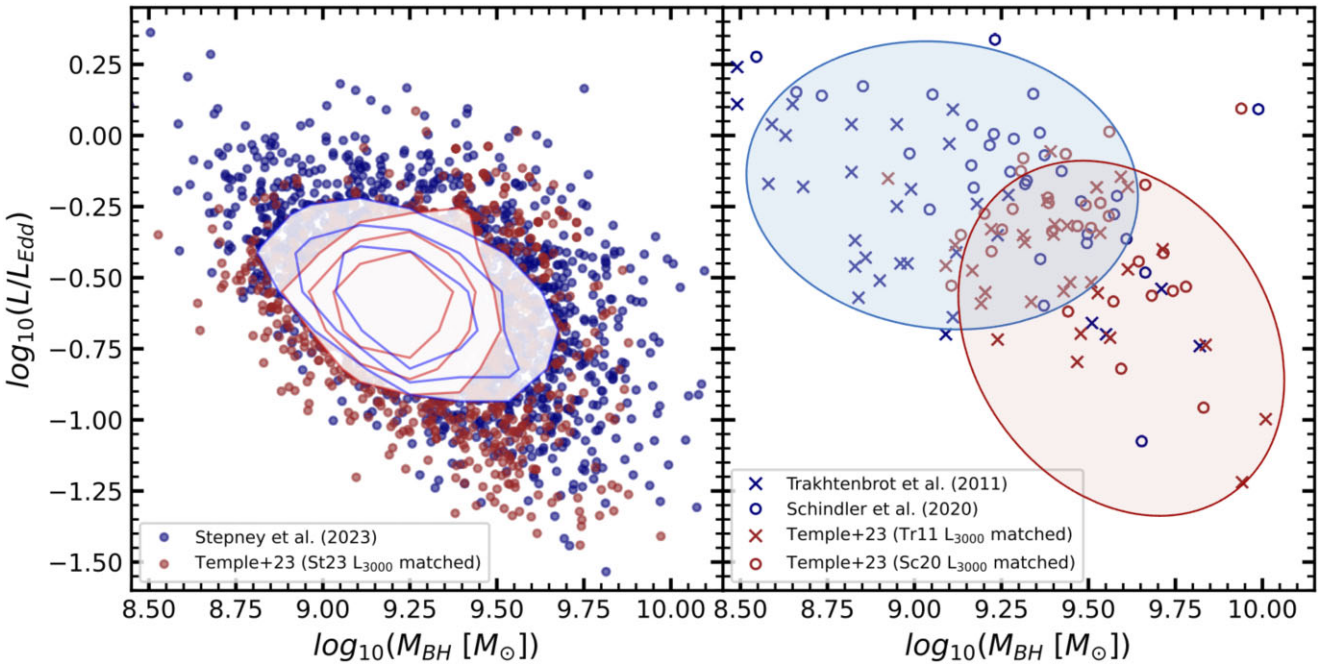

Figure 12. The $M_{\rm BH}$–$L/L_{\rm Edd}$ plane for the $3.5 < z < 4.0$ and corresponding UV luminosity matched $1.5 < z < 2.65$ samples (left-hand panel) and the z∼6 and corresponding UV luminosity-matched $1.5 < z < 2.65$ samples (right-hand panel). Density contours (left-hand panel) encircle 68 per cent, 50 per cent, and 25 per cent of the sample, respectively. The cartoon ellipses (right-hand panel) approximate the locations of the $z \sim 6$ quasars (blue) and the $1.5 < z < 2.65$ quasars, when UV luminosity matched to the $z \sim 6$ sample (red). When UV luminosity matching the $3.5 < z < 4.0$ sample to the $1.5 < z < 2.65$ quasars, the samples are consistent in the $M_{\rm BH}$–$L/L_{\rm Edd}$ plane, explaining the results presented in Figs 5 and 6. When UV luminosity matching the z∼6 sample to the $1.5 < z < 2.65$ quasars, we see an inconsistency between the samples in the $M_{\rm BH}$–$L/L_{\rm Edd}$ plane, with the $z \sim 6$ objects biased towards higher $L/L_{\rm Edd}$ and lower $M_{\rm BH}$ than their $1.5 < z < 2.65$ counterparts.

This is perhaps unsurprising when one considers the degeneracy in matching quasar samples through their luminosities, i.e. samples with low Eddington-scaled accretion rates and high SMBH masses will populate the same region of the luminosity distribution as samples with high Eddington-scaled accretion rates and low SMBH masses. As there are relatively small numbers of $z \sim 5$–7 quasars and they are observed at higher Eddington-scaled accretion rates and lower SMBH masses, a region that is not populated well by the $1.5 < z < 2.65$ sample used as a control, UV-luminosity matching is ineffective in selecting a control sample of quasars with a similar SMBH mass and Eddington-scaled accretion rate distribution as the quasars found at $1.5 < z < 2.65$. Indeed, Farina et al. (2022) do find that the $z > 6$ quasars have systematically higher Eddington-scaled accretion rates compared to a UV-luminosity matched control sample at lower redshifts. Regardless of whether this is an intrinsic property of the highest redshift quasar population or a selection bias in the observed samples, this could in part explain the observed discrepancies in the C IV blueshifts between $1.5 < z < 2.65$ and $z \gtrsim 6$ quoted in the literature.

It is curious then, when exploring the trends in Fig. 10, that an extrapolation of these trends would imply that the lower mass, higher Eddington-scaled accretion rate quasars at $z > 6$ should have higher He II EWs and therefore smaller C IV blueshifts compared to the luminosity-matched control at $1.5 < z < 2.65$, contrary to what is observed. Unfortunately the He II EWs have not been measured for the highest redshift quasars, which precludes any direct comparison to the $3.5 < z < 4.0$ sample analysed here. In the case of the $3.5 < z < 4.0$ sample, our use of the novel MFICA technique has enabled us to extract information about the He II EWs even for spectra of modest signal-to-noise. While we do not have information on the He II properties at the highest redshifts, several papers have looked at the X-ray properties of the highest redshift quasars and confirmed the well-known correlation between $\alpha_{\rm OX}$, the UV-to-X-ray SED slope, and the UV luminosity. Higher luminosity quasars have proportionally lower X-ray flux and therefore softer ionizing SEDs with no apparent evolution in $\alpha_{\rm OX}$ with redshift (Nanni et al. 2017; Pons et al. 2020).

If the trends illustrated in Fig. 10 do break down for the $z \sim 6$ population, this might point to a change in the underlying mechanisms driving the C IV blueshift. Meyer et al. (2019) have speculated about the role of orientation and obscuration in explaining the apparent lack of $z > 6$ quasars with modest blueshifts. In a flux-limited sample probing only the highest UV-luminosity sources, quasars that are viewed more edge-on and/or more obscured would preferentially drop out of the sample. If the wind geometry is polar, these missing quasars would also be those at more modest blueshifts, thus explaining the bias to high blueshifts at $z > 6$. Our work now explicitly demonstrates that despite sampling higher UV-luminosity sources at $3.5 < z < 4.0$, there is no such bias in their C IV emission line properties relative to $z \sim 2$, which could imply that the geometry and obscured fraction of quasars dramatically changes from $z \sim 4$ to $z \gtrsim 6$. Alternatively, it might be inappropriate to extrapolate the trends in Fig. 10 to the super-Eddington regime given the inner accretion disc transitions from geometrically thin and optically thick to a slim disc as radiation pressure causes the disc to 'puff up' (Giustini & Proga 2019).

It is also important to highlight that when illustrating trends in Fig. 12, all the SMBH masses, luminosities, and Eddington-scaled accretion rates for the Trakhtenbrot et al. (2011) sample were re-derived using equations (2) and (3). Although we currently take the

equivalent properties for the $z \gtrsim 6$ quasars directly from Schindler et al. (2020), our results would remain unchanged if we used the continuum luminosities and FWHM of the emission lines from that paper to re-derive black hole masses and Eddington-scaled accretion rates for the $z > 6$ sample. Considerable care has also been taken in this work to ensure that the $3.5 < z < 4.0$ and $1.5 < z < 2.65$ samples have employed the same methodologies for calculating quasar systemic redshifts and measuring UV line properties. This was beyond the scope of this paper for the quasar samples analysed at higher redshifts and might result in biases when comparing to the lower redshift population (see e.g. Appendix B).

A key conclusion of our study is that, under the premise that the C IV emission line blueshift is tracing the velocity of radiatively driven disc winds, the fundamental parameters that govern the blueshift are the SMBH mass and Eddington-scaled accretion rate. We have shown that quasars at the highest redshifts do not map on to the SMBH mass Eddington-scaled accretion rate plane occupied by similarly luminous quasars at lower redshifts. A more complete sampling of this plane is clearly needed at $z > 6$ to determine whether the observed evolution in UV-line properties is due to an intrinsic difference in the masses and accretion rates of the first quasars, or conversely, if different mechanisms are at play in driving the observed C IV blueshift compared to quasars at $1.5 < z < 4.0$. This is now becoming possible with the launch of the *JWST* which will enable lower mass, lower accretion rate quasars to be found in the very early Universe, as well as robustly measuring black hole masses and accretion rates for known $z > 6$ quasars using Balmer lines, which suffer considerably less from systematic biases.

6 CONCLUSIONS

We have analysed the rest-frame UV spectra of 2531 ($3.5 < z < 4.0$) quasars from the SDSS DR16Q catalogue and studied the evolution of the rest-frame UV properties of quasars in the redshift range $1.5 < z < 4.0$.

(i) We used high signal-to-noise template spectra of quasars at $1.5 < z < 3.5$ and a cross-correlation algorithm to calculate updated systemic redshifts for the $3.5 < z < 4.0$ quasars. The templates take into account the known systematic velocity offsets between different emission lines as a function of quasar properties as well as the diversity of the C IV emission line morphologies. This enables accurate systemic redshift estimates using just the rest-frame UV, a technique that can now be applied to quasars at even higher redshifts.

(ii) We use MFICA to produce high signal-to-noise reconstructions of the individual quasar spectra from which we measure non-parametric emission line properties. We recover the same trends in C IV EW and C IV blueshift as those reported at $1.5 < z < 2.65$. We find that there is no evidence for evolution in the C IV blueshifts and EWs between $1.5 < z < 2.65$ and $3.5 < z < 4.0$ when matching the quasars in either UV continuum luminosity, L_{3000}, or *both* SMBH mass and Eddington-scaled accretion rate.

(iii) The use of MFICA enables us to reconstruct the He II emission line profile even in modest signal-to-noise spectra. We recover the well-known correlation between the He II and C IV EWs as well as an anticorrelation between the He II EW and C IV blueshift. Under the assumption that the C IV blueshift traces BLR outflows, we conclude that the quasar SED and more specifically the ionizing flux above 54 eV is a key determinant of the ability to launch outflows. Moreover, there is a common SED-dependent mechanism for quasar-driven outflows at play in quasars over the entire redshift range $1.5 < z < 4.0$.

(iv) We examine how the rest-frame UV line properties depend on fundamental properties of the quasars—namely L_{3000}, $M_{\rm BH}$, and $L/L_{\rm Edd}$. The $3.5 < z < 4.0$ quasars are more luminous than the $1.5 < z < 2.65$ quasars but show the same trends in their emission line properties with SMBH mass and Eddington-accretion rate as their lower redshift counterparts. As reported by Temple et al. (2023), significant C IV blueshift measurements require *both* $L/L_{\rm Edd} \geq 0.2$ and $M_{\rm BH} \geq 10^9$ M$_\odot$. Likewise, when $L/L_{\rm Edd} \geq 0.2$, we observe a clear evolution in the He II EW, with higher SMBH mass objects presenting both weaker He II emission and larger C IV blueshifts.

(v) We explicitly show that matching quasars at $3.5 < z < 4.0$ to those at $1.5 < z < 2.65$ based on their UV continuum luminosity, ensures a consistent mapping of quasars in both redshift bins on to the $M_{\rm BH}$–$L/L_{\rm Edd}$ plane. However, when considering the much smaller sample of quasars at $z \sim 5$–7 where UV-emission line properties have been measured, the UV-luminosity matched $1.5 < z < 2.65$ samples are biased to higher SMBH mass and lower Eddington-scaled accretion rates than observed at the highest redshifts. If SMBH mass and Eddington-scaled accretion rate are indeed the fundamental parameters driving the C IV blueshift, this might at least partially explain the observed evolution of C IV blueshift seen in the highest redshift quasars. We therefore conclude that matching quasar samples in different redshift bins using the UV continuum luminosity is only viable when one can also achieve a reasonable match in *both* the SMBH mass and Eddington-scaled accretion rate.

(vi) We hypothesize a number of explanations for the inconsistent distributions in the $M_{\rm BH}$–$L/L_{\rm Edd}$ plane between $1.5 < z < 4.0$ and $z \sim 5$–7. Farina et al. (2022) find that quasars at $z \gtrsim 6$ have a tendency towards higher Eddington-scaled accretion rates and lower SMBH masses than their $1.5 < z < 2.65$ UV luminosity-matched counterparts. Interestingly, if the relationship between the He II EW and the $M_{\rm BH}$–$L/L_{\rm Edd}$ plane persists to $z \sim 5$–7, we would expect objects with higher Eddington-scaled accretion rates and lower SMBH masses to exhibit weaker C IV blueshifts. This trend is contrary to the observations at $z \gtrsim 6$, for which we suggest two possible explanations. One possibility is that the relationships between the $M_{\rm BH}$, $L/L_{\rm Edd}$, and the UV emission line properties, at $1.5 < z < 4.0$, do not hold at higher redshifts where the Eddington ratios appear higher, and hence the mechanisms driving outflows at $z \gtrsim 6$ are intrinsically different. Alternatively, the different line-fitting methodologies used to analyse the quasar samples at $z \gtrsim 6$ may prevent a direct comparison to the UV emission line properties at more modest redshifts.

ACKNOWLEDGEMENTS

We thank Prof. Christian Knigge and the anonymous referee for their useful comments that helped strengthen the work.

MS acknowledges funding from the University of Southampton via the Mayflower studentship. MB acknowledges funding from the Royal Society via a University Research Fellowship (UF160074). MJT acknowledges support from a FONDECYT postdoctoral fellowship (3220516). ALR acknowledges support from UKRI (MR/T020989/1). For the purpose of open access, the author has applied a Creative Commons Attribution (CC BY) licence to any Author Accepted Manuscript version arising from this submission.

Funding for the Sloan Digital Sky Survey IV has been provided by the Alfred P. Sloan Foundation, the U.S. Department of Energy Office of Science, and the Participating Institutions. SDSS-IV acknowledges support and resources from the Center for High-

Performance Computing at the University of Utah. The SDSS web site is www.sdss.org.[3]

SDSS-IV is managed by the Astrophysical Research Consortium for the Participating Institutions of the SDSS Collaboration including the Brazilian Participation Group, the Carnegie Institution for Science, Carnegie Mellon University, the Chilean Participation Group, the French Participation Group, Harvard-Smithsonian Center for Astrophysics, Instituto de Astrofísica de Canarias, The Johns Hopkins University, Kavli Institute for the Physics and Mathematics of the Universe (IPMU)/University of Tokyo, the Korean Participation Group, Lawrence Berkeley National Laboratory, Leibniz Institut für Astrophysik Potsdam (AIP), Max-Planck-Institut für Astronomie (MPIA Heidelberg), Max-Planck-Institut für Astrophysik (MPA Garching), Max-Planck-Institut für Extraterrestrische Physik (MPE), National Astronomical Observatories of China, New Mexico State University, New York University, University of Notre Dame, Observatário Nacional/MCTI, The Ohio State University, Pennsylvania State University, Shanghai Astronomical Observatory, United Kingdom Participation Group, Universidad Nacional Autónoma de México, University of Arizona, University of Colorado Boulder, University of Oxford, University of Portsmouth, University of Utah, University of Virginia, University of Washington, University of Wisconsin, Vanderbilt University, and Yale University.

DATA AVAILABILITY

The spectroscopic data underlying this article are available from SDSS.[4]

REFERENCES

Alexander D. M. et al., 2023, AJ, 165, 124
Allen J. T., Hewett P. C., Richardson C. T., Ferland G. J., Baldwin J. A., 2013, MNRAS, 430, 3510
Bañados E. et al., 2016, ApJS, 227, 11
Baskin A., Laor A., Stern J., 2013, MNRAS, 438, 604
Baskin A., Laor A., Hamann F., 2015, MNRAS, 449, 1593
Bischetti M. et al., 2022, Nature, 605, 244
Bischetti M. et al., 2023, ApJ, 952, 44
Brodzeller A., Dawson K., 2022, AJ, 163, 110
Coatman L., Hewett P. C., Banerji M., Richards G. T., 2016, MNRAS, 461, 647
Coatman L., Hewett P. C., Banerji M., Richards G. T., Hennawi J. F., Prochaska J. X., 2017, MNRAS, 465, 2120
Dawson K. S. et al., 2012, AJ, 145, 10
Dawson K. S. et al., 2016, AJ, 151, 44
De Rosa G. et al., 2014, ApJ, 790, 145
Fan X., Banados E., Simcoe R. A., 2022, preprint (arXiv:2212.06907)
Farina E. P. et al., 2022, ApJ, 941, 106
Foreman-Mackey D., Hogg D. W., Lang D., Goodman J., 2013, PASP, 125, 306
Giustini M., Proga D., 2019, A&A, 630, A94
Goodman J., Weare J., 2010, Commun. Appl. Math. Comput. Sci., 5, 65
Hewett P. C., Wild V., 2010, MNRAS, 405, 2302
Højen-Sørensen P. A., Winther O., Hansen L. K., 2002, Neural Comput., 14, 889
Jiang L. et al., 2016, ApJ, 833, 222
Kulkarni G., Worseck G., Hennawi J. F., 2019, MNRAS, 488, 1035
Lyke B. W. et al., 2020, ApJS, 250, 8
Maddox N., Hewett P. C., Péroux C., Nestor D. B., Wisotzki L., 2012, MNRAS, 424, 2876
Mathews W. G., Ferland G. J., 1987, ApJ, 323, 456
Mazzucchelli C. et al., 2017, ApJ, 849, 91
Merloni A. et al., 2019, The Messenger, 175, 42
Meyer R. A., Bosman S. E. I., Ellis R. S., 2019, MNRAS, 487, 3305
Mortlock D. J. et al., 2011, Nature, 474, 616
Nanni R., Vignali C., Gilli R., Moretti A., Brandt W. N., 2017, A&A, 603, A128
Pâris I. et al., 2012, A&A, 548, A66
Pons E., McMahon R. G., Banerji M., Reed S. L., 2020, MNRAS, 491, 3884
Rakshit S., Stalin C. S., Kotilainen J., 2020, ApJS, 249, 17
Rankine A. L., Hewett P. C., Banerji M., Richards G. T., 2020, MNRAS, 492, 4553
Reed S. L. et al., 2019, MNRAS, 487, 1874
Richards G. T. et al., 2011, AJ, 141, 167
Rivera A. B., Richards G. T., Gallagher S. C., McCaffrey T. V., Rankine A. L., Hewett P. C., Shemmer O., 2022, ApJ, 931, 154
Schindler J.-T. et al., 2020, ApJ, 905, 51
Schlafly E. F., Finkbeiner D. P., 2011, ApJ, 737, 103
Schneider D. P. et al., 2010, AJ, 139, 2360
Shen Y. et al., 2011, ApJS, 194, 45
Sulentic J. W., Bachev R., Marziani P., Negrete C. A., Dultzin D., 2007, ApJ, 666, 757
Temple M. J., Hewett P. C., Banerji M., 2021, MNRAS, 508, 737
Temple M. J. et al., 2023, MNRAS, 523, 646
Timlin J. D. I., Brandt W. N., Laor A., 2021, MNRAS, 504, 5556
Trakhtenbrot B., Netzer H., Lira P., Shemmer O., 2011, ApJ, 730, 7
Wang F. et al., 2019, ApJ, 884, 30
Wu Q., Shen Y., 2022, ApJS, 263, 42
Yang J. et al., 2021, ApJ, 923, 262
Yang J. et al., 2023, preprint (arXiv:2302.01777)
Zakamska N. L., Greene J. E., 2014, MNRAS, 442, 784

SUPPORTING INFORMATION

Supplementary data are available at *MNRAS* online.

CompositeSpec.zip
ICAComponents.zip
Stepney_2023_MNRAS.fits

Please note: Oxford University Press is not responsible for the content or functionality of any supporting materials supplied by the authors. Any queries (other than missing material) should be directed to the corresponding author for the article.

APPENDIX A: THE MFICA COMPONENTS

As discussed in Section 3, we reconstruct spectra using MFICA. To account for the broad diversity of the C IV emission line profiles, we require the use of three sets of MFICA components to reconstruct the quasar spectra. The objects whose C IV EW <20 Å were fit using the components depicted in Fig. A1, the objects whose 20 < C IV EW < 70 Å were fit using the components depicted in Fig. A2 and the remainder of the spectra were reconstructed using the components depicted in Fig. A3. The C IV EW thresholds were calculated by minimizing the χ^2_ν of the reconstructions; however, spectra in the overlapping regions of equivalent EW generally have a similar quality fit with either set of MFICA components.

[3] www.sdss.org
[4] https://www.sdss4.org/dr17/

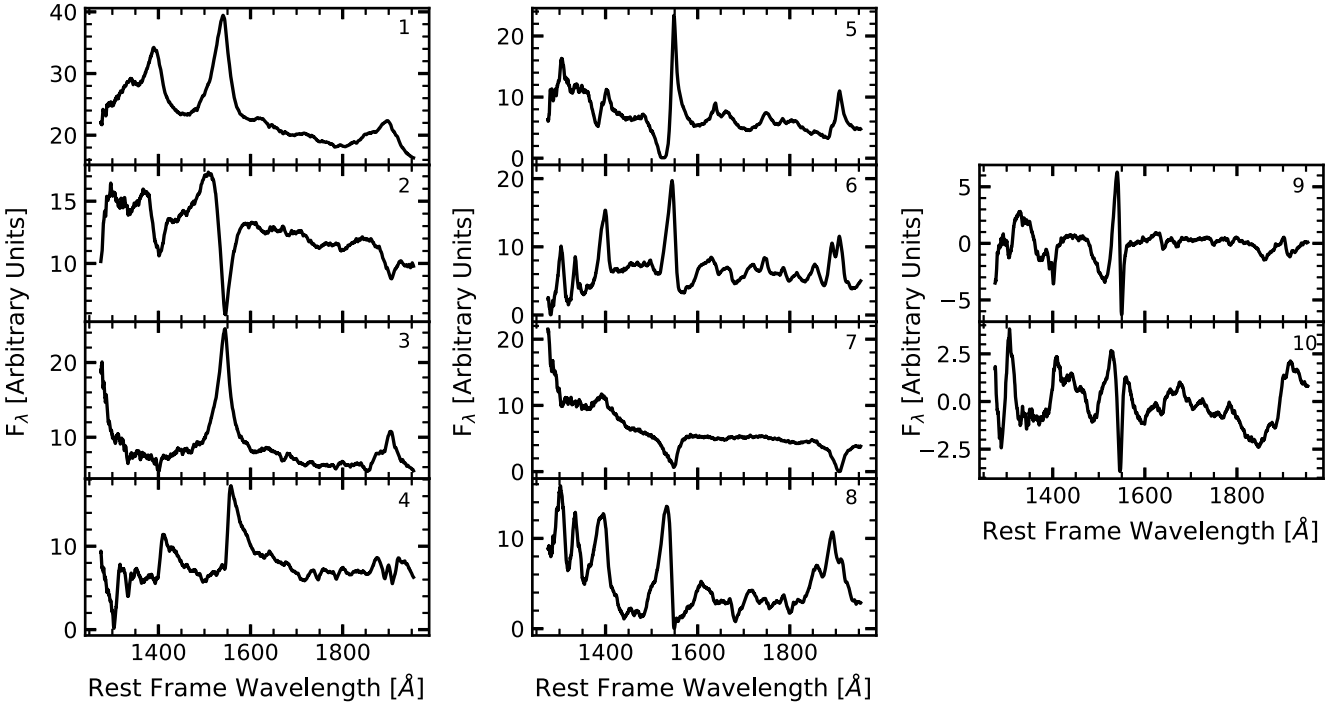

Figure A1. The MFICA components, generated using the technique described in Allen et al. (2013), used to reconstruct quasar spectra whose C IV EW < 20 Å. Components '9' and '10' are correction components and are therefore permitted to have negative weights in the MCMC fitting.

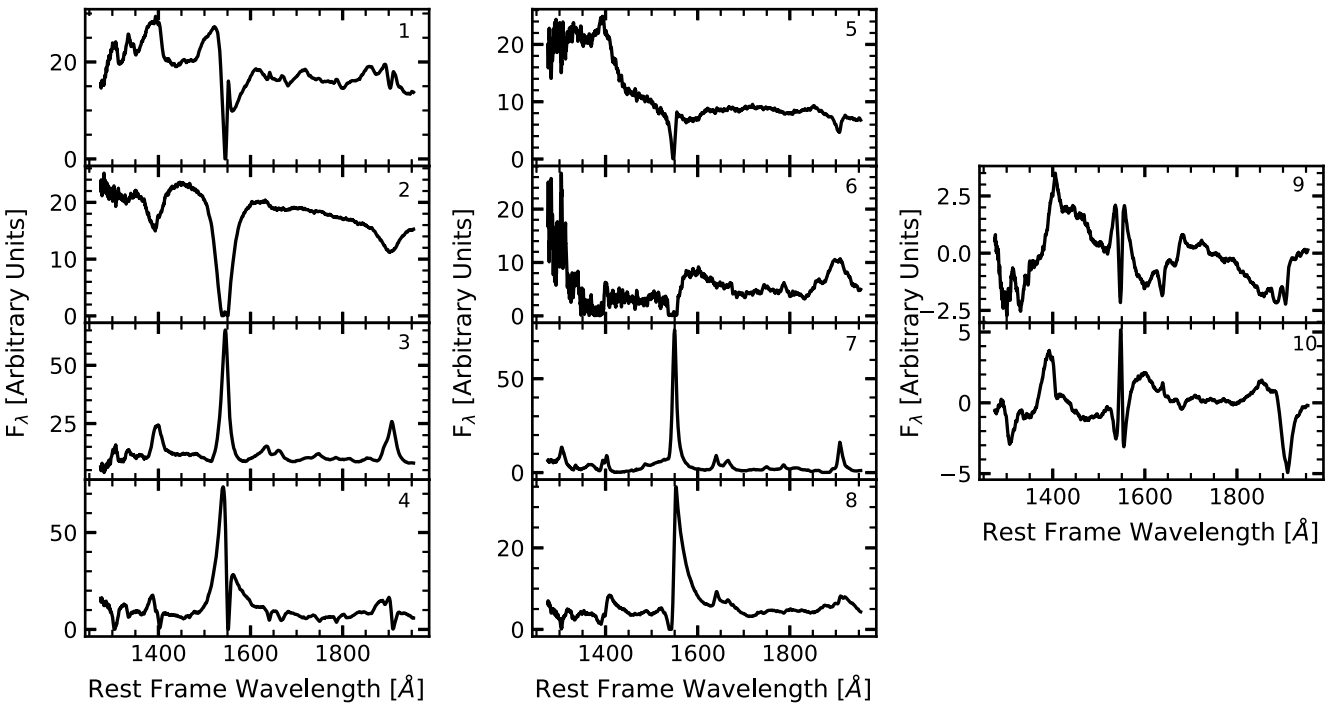

Figure A2. The MFICA components, generated using the technique described in Allen et al. (2013), used to reconstruct quasar spectra whose 20 < C IV EW < 70 Å. Components '9' and '10' are correction components and are therefore permitted to have negative weights in the MCMC fitting.

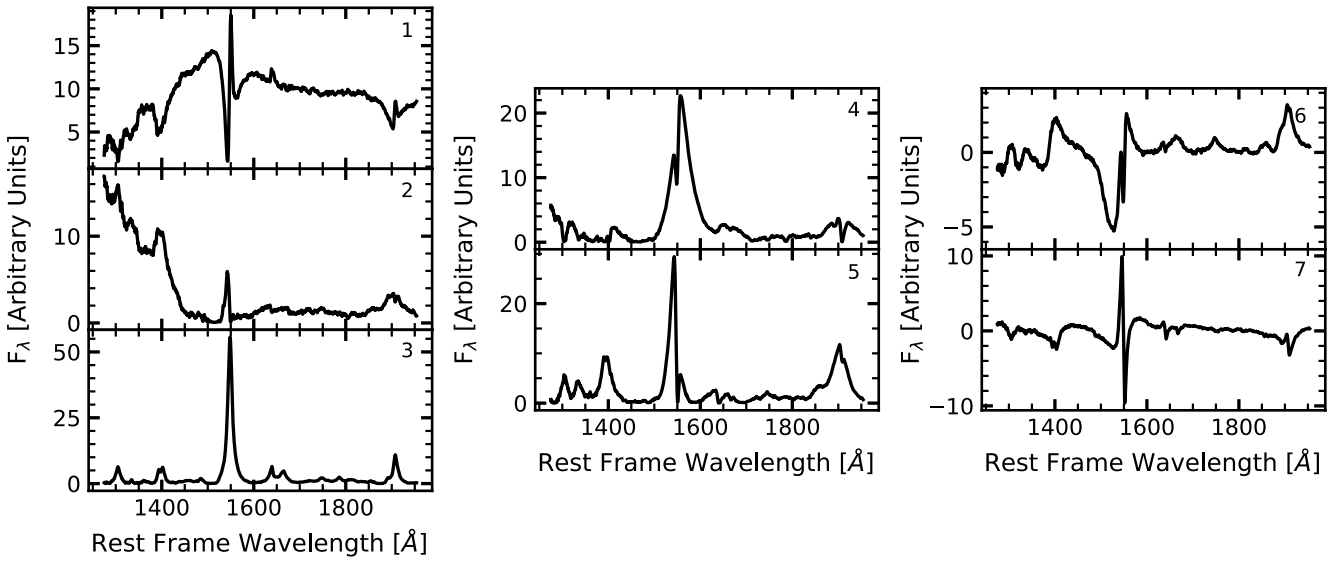

Figure A3. The MFICA components, generated using the technique described in Allen et al. (2013), used to reconstruct quasar spectra whose C IV EW >70 Å. Components '6' and '7' are correction components and are therefore permitted to have negative weights in the MCMC fitting.

APPENDIX B: COMPARISON TO WU & SHEN 2022

Recently Wu & Shen (2022) have published a catalogue of quasar continuum and emission line properties for the ∼750 000 quasars in DR16Q, including updated systemic redshifts for the quasars. Here, we explicitly compare our line properties to theirs. We match the 2531 quasars at $3.5 < z < 4.0$ analysed in this paper to the Wu & Shen (2022) catalogue by position and extract the appropriate rest-frame UV line properties for the comparison.

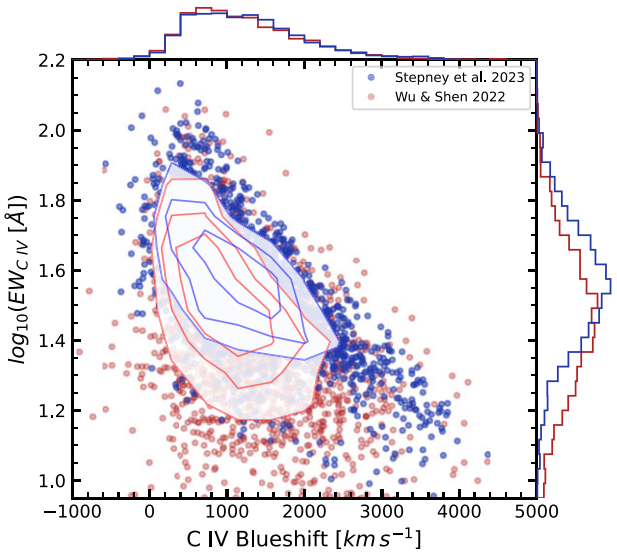

Figure B1. The C IV emission space for the $3.5 < z < 4.0$ sample, using line properties derived from Wu & Shen (2022; red) and this work (blue). C IV blueshifts are calculated from line centroids in both distributions. Density contours encircle 68 per cent, 50 per cent, and 25 per cent of the sample, respectively. Marginalized distributions of the C IV blueshift and EW are also shown. The distributions do not feature the same characteristic shape in C IV emission space, with the Wu & Shen (2022) objects biased to lower C IV EW.

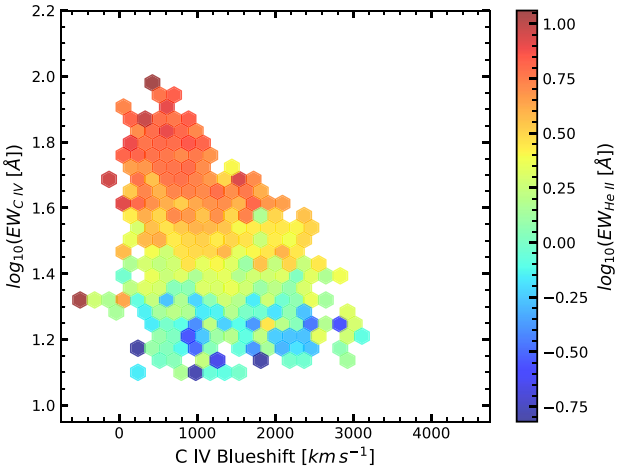

Figure B2. The median observed He II EW in bins of C IV blueshift and C IV EW for the $3.5 < z < 4.0$ sample, using line properties derived from Wu & Shen (2022). The He II EW is correlated with C IV EW; however, the He II EW measurements are systematically overestimated when compared to this work. The correlation between the He II EW and the C IV blueshift is also significantly weaker than what is observed in Fig. 8.

Precision measurements of the C IV emission line properties was not a primary aim of Wu & Shen (2022). Hence a composite Gaussian fitting recipe was adopted to model the emission line profile. The C IV emission space for the $3.5 < z < 4.0$ sample is presented in Fig. B1. While the marginalized distributions in C IV blueshift are consistent with ours, the marginalized distributions in C IV EW suggest that the Wu & Shen (2022) catalogue is biased to lower C IV EW when compared with this work. Since the low C IV EW line profiles are poorly approximated by parametric fitting recipes, the characteristic tail to high blueshifts in the C IV emission space is not as evident when one uses the Wu & Shen (2022) measurements.

A key result of our paper is the correlation presented in Fig. 8. The existence of a correlation between the He II EW and both C IV EW and blueshift could suggest that the C IV emission is tracing outflows

and that these are radiatively driven with an explicit dependence on the ionizing SED. In Fig. B2, we present the same results using the Wu & Shen (2022) measurements. In addition to the bias towards lower C IV EW, the He II EW measurements appear systematically larger than those measured in this work. This difference can, in part, be attributed to the way in which the He II continuum is defined. Finally, while the correlation between He II EW and C IV EW persists, in Fig. B2, the anticorrelation between He II EW and C IV blueshift is significantly weaker. This highlights the strength of the MFICA technique in recovering robust He II EWs and C IV blueshifts for high-redshift quasar spectra.

APPENDIX C: SYSTEMIC REDSHIFT DEPENDENCE ON REST-FRAME WAVELENGTH RANGE

A key aim of this paper was to ensure that quasar samples across the entire redshift range have been analysed with the same methodologies for line-fitting and inference of quasar physical properties. However, at high-redshifts of $3.5 < z < 4.0$, the SDSS spectrum covers a more limited rest-frame wavelength range compared to quasars at $1.5 < z < 2.65$. In this paper, we truncated the $3.5 < z < 4.0$ spectra at 2000 Å before estimating systemic redshifts and reconstructing the line profiles, due to the poor signal-to-noise quality towards the red-most end of the SDSS observed wavelength range. To assess the impact of the restricted wavelength range on systemic redshift estimates, we constructed a random sample of 1000 quasars from the UV luminosity matched $1.5 < z < 2.65$ quasars from Rankine et al. (2020). We then truncated the spectra at 2000 Å and ran our cross-correlation algorithm on these quasars to calculate systemic redshifts. These are then compared to the redshifts estimated by Rankine et al. (2020) over a wider wavelength range in Fig. C1.

The redshift difference is systematic as a function of the C IV blueshift below blueshifts of $\sim 1000\,\mathrm{km\,s^{-1}}$. The algorithm has a tendency to slightly overestimate systemic redshifts for objects whose C IV blueshift $\leq 500\ \mathrm{km\,s^{-1}}$. This is due to the presence of narrow associated absorbers predominantly affecting the C IV lines at low blueshift but which are at low enough signal-to-noise to be not picked up by our narrow absorption masking procedure. As a result, the symmetric C IV line profiles, with the majority of their flux at velocities close to the systemic redshift, are most affected. The implication for the results presented in Figs 5 and 6 is that since the algorithm more readily overestimates the systemic redshift at low C IV blueshift, the position of the line centroid is shifted bluewards as a result, hence the number of objects with C IV blueshift $\leq 500\ \mathrm{km\,s^{-1}}$ tails off more rapidly at $3.5 < z < 4.0$ compared to the lower redshift quasar population. The high C IV blueshift tail on the other hand is less affected by this systemic redshift bias. The conclusions in this paper regarding the evolution of high C IV blueshift quasars are therefore robust.

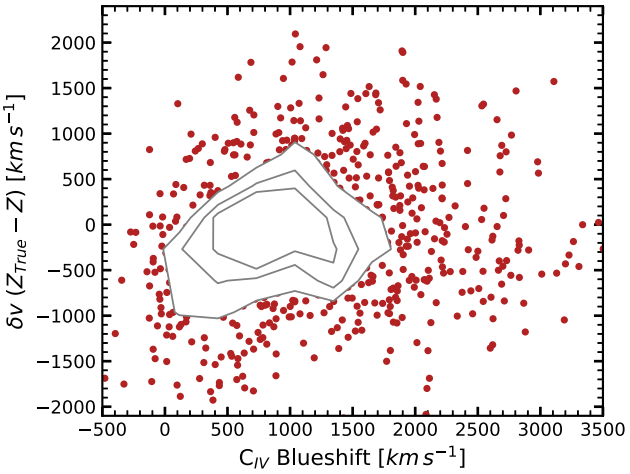

Figure C1. The velocity difference in systemic redshifts between those estimated by Rankine et al. (2020) and calculated using the same recipe and rest-frame wavelength range as this work. This is plotted as a function of the C IV blueshift for a random sample of 1000 ($1.5 < z < 2.65$) quasars of comparable luminosity to the $3.5 < z < 4.0$ quasar population. At low C IV blueshifts, the cross-correlation algorithm has a tendency to overestimate the systemic redshift and therefore biases the C IV line centroids bluewards of their true position.

This paper has been typeset from a TEX/LATEX file prepared by the author.